UCID- 17241

Lawrence Livermore Laboratory

STRUCTURAL RESPONSE CALCULATIONS FOR A REVERSE BALLISTICS TEST OF AN EARTH PENETRATOR

D. F. Alves and G. L. Goudreau

August 1976

Prepared for U.S. Energy Research & Development Administration under contract No. W-7405-Eng-48.

DISCLAIMER

STRUCTURAL RESPONSE CALCULATIONS FOR A REVERSE BALLISTICS TEST OF AN EARTH PENETRATOR

D. F. Alves and G. L. Goudreau
Lawrence Livermore Laboratory, University of California
Livermore, California

A dynamic response calculation has been performed on a half-scale earth penetrator to be tested on a reverse ballistics test in August 1976. In this test a 14 inch diameter sandstone target is fired at the EP at 1800 ft/sec at normal impact. Several other calculators are independently attempting to predict the internal structural response of the penetrator based on the loading conditions predicted by California Research and Technology (CRT), who modeled a rigid body penetrating the sandstone media.

Basically two types of calculations were made. The first utilized an axisymmetric, finite element code DTVIS2 in the dynamic mode and with materials having linear elastic properties. CRT's radial and axial force histories were smoothed to eliminate grid encounter frequency and applied to the nodal points along the nose of the penetrator. Given these inputs DTVIS2 then calculated the internal dynamic response. Secondly, SAP4, a structural analysis code, is utilized to calculate axial frequencies and mode shapes of the structure. A special one dimensional display facilitates interpretation of the mode shape. DTVIS2 and SAP4 use a common mesh description.

Special considerations in the calculation are the assessment of the effect of gaps and preload and the internal axial sliding of components.

OT W-7405-ENG-48

The earth penetrator and internal components were built by Sandia Laboratories in Albuquerque, New Mexico (see Fig. 1). This 47 pound penetrator is 32 inches long and has a diameter that flares from 3 inches to 3.35 inches. This penetrator is extensively instrumented; having 5 active longitudinal accelerometers, 2 passive accelerometers, and 36 strain gages. Location of the accelerometers and strain gages are shown in Fig. 1. A potting compound, MICA-50, was used as a filler throughout the interior of the penetrator to support the components during deceleration. This potting compound was developed by Sandia Laboratories and supplied to Terra Tek (1) for testing to determine its mechanical properties.

Each potted assembly is made independent of the component can and is then centered on the tee rings (see Fig. 1). These tee rings are then torqued to approximately 10 ft-lb, corresponding to a nominal preload of 250 lb. Once the individual cans are in place the aft ring is then torqued to 50 ft-lb resulting in a 1000 pound preload. As a result of machining difficulties there is a gap of 0.005 inch to 0.015 inch between the case and the steel liner (2).

The reverse ballistics test will be performed by AVCO Corporation. The target consists of a layered cylinder as shown in Fig. 2. The test assembly consists of a 14 inch diameter cylinder of sandstone, placed in a thin-wall aluminum can with outside diameter of 15.18 inch and a wall thickness of 0.09 inch. A 0.5 inch gap between the sandstone and the can is filled with a Portland cement matching grout. The sandstone cylinder is 9 inches long with a 1 inch layer of sand on a 1.5 inch aluminum backplate for a total length of 11.5 inches.

In order to determine the structural response of the earth penetrator, LLL, as well as other calculators, had to rely on the calculated loading inputs from California Research and Technology (3). CRT's WAVE-L code, a two

dimensional code that solves the equations of motion for elastic-plastic bodies through a finite-difference Lagrangian technique, was used for the penetration calculation. The penetrator was assumed to be a rigid body. A total of 57 lattice points were used along the penetrator periphery. An axial spacing of 1/2 inch was used along the conical nose tip and 1/8 inch along the ogive section. The penetration calculation was carried out to a time of 465 microseconds and a depth of 9.86 inches. The results of the calculations are in the form of axial and radial force time histories of the 57 points along the penetrator surface. These force histories were smoothed to eliminate the loading oscillations resulting from the projectile's successive encounters with each row of cells throughout the penetration.

The smoothed force time histories were used in our computer model. The zoning in the nose of the EP was modified to correspond to every one in CRT's model for the first 17 node points at the front and then to every other one of CRT's points for the remaining points back to the tangent point. The histories were digitized in a suitable format for our code input. After several preliminary runs with DTVIS2, it became apparent that the initial rise times of many nodal force time histories were too fast and resulted in extremely noisy plots. Therefore the force time histories were modified to eliminate the fast rise times by sampling the histories at 25 microsecond steps. This effectively eliminated all rise times faster than 25 microseconds. An example of CRT's unfiltered histories, smoothed histories, and our interpretation are shown in Fig. 3.

The analysis was performed with the aid of two codes, DTVIS2 and SAP4. A finite element code, DTVIS2, was used in the linear elastic and dynamic mode to determine acceleration, stress, and strain histories. SAP4, a structural analysis code, was utilized to determine axial mode shapes of the entire penetrator and some internal components.

The DTVIS2 model, consisting of 700 elements and 837 nodes, is shown in Fig. 4. The calculation was carried out to 1000 microseconds. Since CRT's load input lasted for the first 465 microseconds, the load was released linearly from 465 to 600 microseconds to prevent any shock unloading. Each component can is separated by a 0.050 inch air gap and is connected (bonded) to the inside liner at the corners. There is a layer between the component can and the liner. Whenever there is a layer or gap there are basically 4 ways to interpret the layer effects. These are:

1. Released A released layer cannot transmit any force between the adjacent components (i.e., an air gap that does not close).
2. Bonded A bonded layer can transmit both normal and tangential forces between adjacent components (i.e., a welded or glued component).
3. Shearless A shearless layer can transmit normal forces but can not transmit tangential forces between adjacent component (i.e., a greased layer). This is done by setting the shear modulus equal to zero. By increasing the shear modulus an artificial friction may be added to this type of layer.
4. One-Way A one-way layer can transmit normal compressive forces but cannot transmit normal tensile forces and may or may not transmit tangential forces between adjacent components. (This type of material is not linear and therefore is costly to apply in DTVIS2.)

Rather than attempt to use a "one-way" material, one can determine by preliminary runs whether a component will separate or remain attached to another component. If the two components remain in contact (in compression) throughout the calculation then one can use either a bonded or shearless layer.

Similarly, if the two components tend to separate (in tension) throughout the calculation then a released layer, or air gap, can be used. There are 3 layers in the DTVIS2 model of the EP. These are: between the component cans and the steel liner; between the steel liner and the outside case; and between the D-38 ballast and the case.

Another area of concern that developed in the calculations is whether or not to use a preload. From the initial calculations and preliminary runs it was determined that the actual preload to be used is not large enough to overcome the deceleration loads. This was determined by inspecting the stress levels in the aft potting and comparing this tensile stress with the estimated preload stresses. The results showed the tensile stress levels to be an order of magnitude larger than the compressive stress level due to the preload. Since the preload would not hold the loading, the aft potting was released from the aft titanium bulkhead and allowed to slump. Similarly the preload on the aft ring was not large enough for the loading. Therefore, the inside liner was released from the aft ring and allowed to slump.

Four cases were run on DTVIS2 in order to understand the effects of the layer material. These runs and their differences are tabulated below.

	511	512	513	514
Aft potting and liner	Bonded	Released	Released	Released
Aft ring and liner	Bonded	Released	Released	Released
Liner and case	Shearless	Shearless	Released	Released
Liner and components	Shearless	Released	Released	Released
Ballast and case	Shearless	Bonded	Shearless	Bonded

Run 511 assumes that the preload is sufficient and there is no separation of the potting and bulkhead or of the liner and aft ring. In this run the liner can interact radially with internal components and with the case. There is no friction between the ballast and case.

Run 512 assumes that the preload is not sufficient and the potting and bulkhead as well as the liner and aft ring have separated. The liner interacts radially with the case but is connected to the internal components only at the tee rings. Friction is allowed to develop between the ballast and the case (i.e., that interface is modelled as bonded).

Run 513 also assumed that the preload is not sufficient. The liner is released from both case and internal components (except at tee rings). Also, there is no friction between the ballast and the case.

Run 514 also assumes that the preload is not sufficient and the liner is released. However, friction is allowed to develop between ballast and case.

After further analysis and discussion with Sandia Albuquerque, it was determined that the preload would not be sufficient to prevent a gap from opening between the liner and the aft cap and that the interference fit of the ballast in the case would be sufficient to prevent the ballast from slipping. One key problem remained unresolved. The interaction of the liner and the case was uncertain. During the deceleration, or even during the application of the preload, the liner may slump and bottom out on the base in the tapered region. Since there is much uncertainty in the actual gap size, it is difficult to assess this problem. Therefore the resulting plots will show the effect of the liner interacting with the case.

Despite the differences among the four runs, several fundamental conclusions can be made. It is the basic differences among these runs, however, that reveal insights into the structural behavior of the penetrator. DTVIS2 predicts that the sandstone target accelerate the penetrator to 70 ft/sec (Fig. 5) in the first 500 microseconds of penetration with a peak rigid body acceleration of 6800 g's (Fig. 6). The acceleration history of the forward accelerometer produces so much noise that the rigid body acceleration is lost (Fig. 7).

After 150 microseconds of penetration, however, the liner begins to separate from the rear cap (Fig. 8). This separation increases to 90 mils and the liner and cap do not rebound until 550 microseconds of penetration. The stress associated with a preload required to prevent such a gap opening would be 120,000 psi. Such a preload would result in an inefficient penetration design since the liner and other associated components would have to survive large compressive stresses as well as the preload stress. When the liner is allowed to interact with the case, the tendency of the gap opening is reduced since the tapered region of the liner is allowed to bear on the case. The overall compression of the liner is reduced 10% when it is allowed to interact with the case (Figs. 9 and 10).

Perhaps the most significant effect of the interacting liner can be seen in the hoop strain of the liner along the taper (Fig. 11). When the liner does not interact with the case, tensile hoop strains develop from a Poisson effect from the large axial compressive state. However, when the liner is allowed to interact with the case, compressive hoop strains develop since the liner is compressed radially by "wedging" itself along the taper.

The axial strains on the outside of the case are not influenced by the liner (Fig. 12). However, the hoop strains increase on the outside case since the liner is allowed to "push" radially on the case along the taper (Fig. 13).

Additional plots are added in the Appendix for detail of the first 500 microseconds. Also multiplots are included for easy comparison between different components.

In order to look at mode shapes and to calculate axial frequencies, a structural analysis code, SAP4, was utilized. Using the same mesh as DTVIS2, SAP4 calculated the frequencies for the first 6 mode shapes. These are tabulated below. The radial interaction of the liner and case tend to stiffen the structure causing the fundamental frequency to go from 1227 cps for noninteracting sides to 2120 cps for interacting sides. By tieing the aft section to the case, the fundamental frequency increases further to 2550 cps.

Mode	A Tied Rear Interacting Sides Nose Friction	B Untied Rear Interacting Sides Nose Friction	C Untied Rear Interacting Sides No Nose Friction	D Untied Rear Noninteracting Sides Nose Friction
1	0 cps	0 cps	0 cps	0 cps
2	2450	2120	2110	1227
3	3660	3140	2920	2846
4	4220	3740	3730	3501
5	4750	4350	4340	4037
6	5560	5200	4920	4672

There are seven nodal paths shown in Fig. 18. The relative axial modal displacement of each node along each of these paths are plotted against its

axial station for the first six mode shapes in Figs. 19 to 23. Mode shape 1 is ignored since it refers to rigid body motion. In Figure 19c the liner (curve 2) tends to behave in the same way as the internal components (curves 3 - 7). The large difference at the rear between the case (curve 1) and the liner demonstrates the tendency of the liner to slump and separate from the preload cap. In the higher mode shapes, there is a large increase in the mode shape of the forward accelerometer (curve 4). This reveals that there is a high frequency (3700 to 4600 cps) excitation in the accelerometer mounting plate. Furthermore, a large increase in mode shapes of both aft cap and aft bulkhead (curves 1 and 2) can be seen in Fig. 23. This implies that the aft cap and bulkhead will be excited at 5000 cps. The mode shapes in the upper left "a" figures show how the tied rear plate stiffens the whole system into an integrated bar. This case exhibits what would be observed in a typical shaker table sweep, where the low amplitude exitation would not unload the preload. Such test data would not give useful insight into the high amplitude penetration environment.

REFERENCES

1. Dropek, R. K., Butters, S. W. and Jones, A. H., "Some Mechanical Properties of MICA-50 Potting Compound," TR 76-4, Defense Nuclear Agency, Washington, D.C., prepared by Terra Tek.

2. McCoy, D. L., a correspondence to all calculators, Feb. 27, 1976, Sandia Laboratories, Albuquerque.

3. Wagner, M. H., Fulton, C. C. and Goerke, W. S., "Calculation of Reverse Ballistic Test into Dakota Sandstone at 1800 ft/sec," Contract DNA 001-76-C-0157, Feb. 1976, Defense Nuclear Agency, Washington, D.C.; prepared by California Research and Technology, Inc.

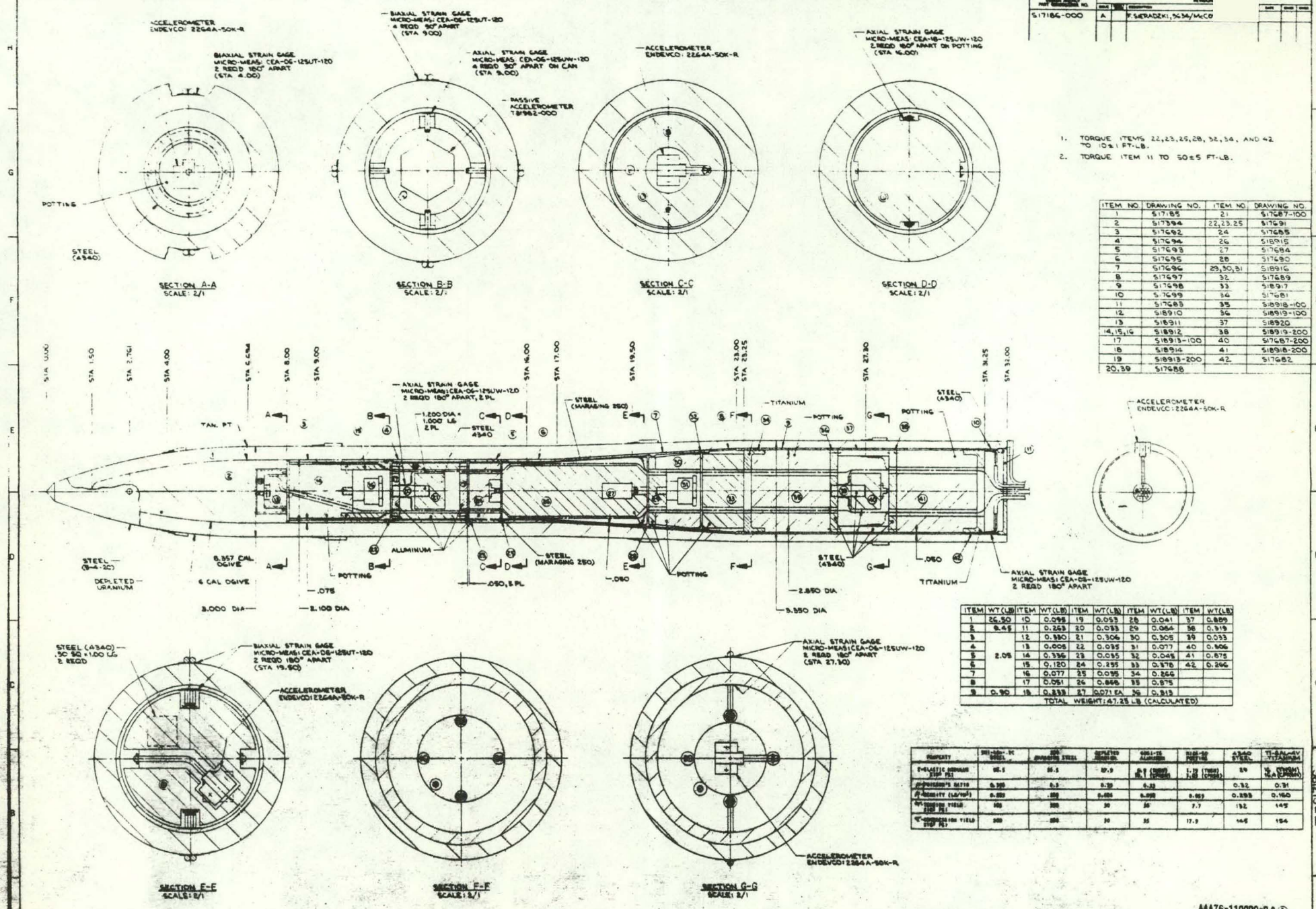

1. TORQUE ITEMS 22,23,25,28, 32, 34, AND 42 TO 10±1 FT-LB.
2. TORQUE ITEM 11 TO 50±5 FT-LB.

ITEM NO.	DRAWING NO.	ITEM NO.	DRAWING NO.
1	S17185	21	S17687-100
2	S17394	22,23,25	S17691
3	S17682	24	S17685
4	S17694	26	S18915
5	S17693	27	S17684
6	S17695	28	S17690
7	S17696	29,30,31	S18916
8	S17697	32	S17689
9	S17698	33	S18917
10	S17699	34	S17681
11	S17683	35	S18918-100
12	S18910	36	S18919-100
13	S18911	37	S18920
14,15,16	S18912	38	S18919-200
17	S18913-100	40	S17687-200
18	S18914	41	S18918-200
19	S18913-200	42	S17682
20,39	S17688		

ITEM	WT (LB)	ITEM	WT (LB)	ITEM	WT (LB)	ITEM	WT (LB)	ITEM	WT (LB)
1	26.50	10	0.095	19	0.053	28	0.041	37	0.889
2	9.45	11	0.253	20	0.033	29	0.084	38	0.319
3		12	0.550	21	0.306	30	0.305	39	0.033
4		13	0.008	22	0.035	31	0.077	40	0.906
5	2.05	14	0.396	23	0.035	32	0.048	41	0.875
6		15	0.120	24	0.255	33	0.378	42	0.266
7		16	0.077	25	0.095	34	0.266		
8		17	0.051	26	0.866	35	0.875		
9	0.90	18	0.333	27	0.071 EA	36	0.319		
TOTAL WEIGHT: 47.25 LB (CALCULATED)									

PROPERTY	304 STAINLESS STEEL	17-4PH STAINLESS STEEL	DEPLETED URANIUM	6061-T6 ALUMINUM	7075-T6 ALUMINUM	A-4340 STEEL	Ti-6Al-4V TITANIUM
E-ELASTIC MODULUS (10⁶ PSI)	28.5	28.5	29.9	10.1 (SHEAR) 10.4 (TENSION)	10.3 (SHEAR) 10.4 (TENSION)	29	16.4 (SHEAR) 16.6 (TENSION)
μ-POISSON'S RATIO	0.305	0.3	0.29	0.33		0.32	0.31
ρ-DENSITY (LB/IN³)	0.289	.283	0.684	0.098	0.101	0.283	0.160
TENSILE YIELD STRENGTH (KSI)	205	200	50	35	77	132	145
COMPRESSION YIELD STRENGTH (KSI)	205	200	50	35	77	145	154

AAA76-110000-0A A

DNA REVERSE BALLISTIC EP PROPOSAL			
UNCLASSIFIED			
UNCLASSIFIED			
	SIZE E	CODE IDENT. NO. 14213	DWG. NO. S17186
	SCALE 1/1	SHEET 1 OF 1	

DWG. NO. S17186

S17186-000 A P. SKRADZKI, 5636/McCO

OFFICIAL USE

Fig. 1.
Assembly drawing of DNA earth penetrator.

Figure 1

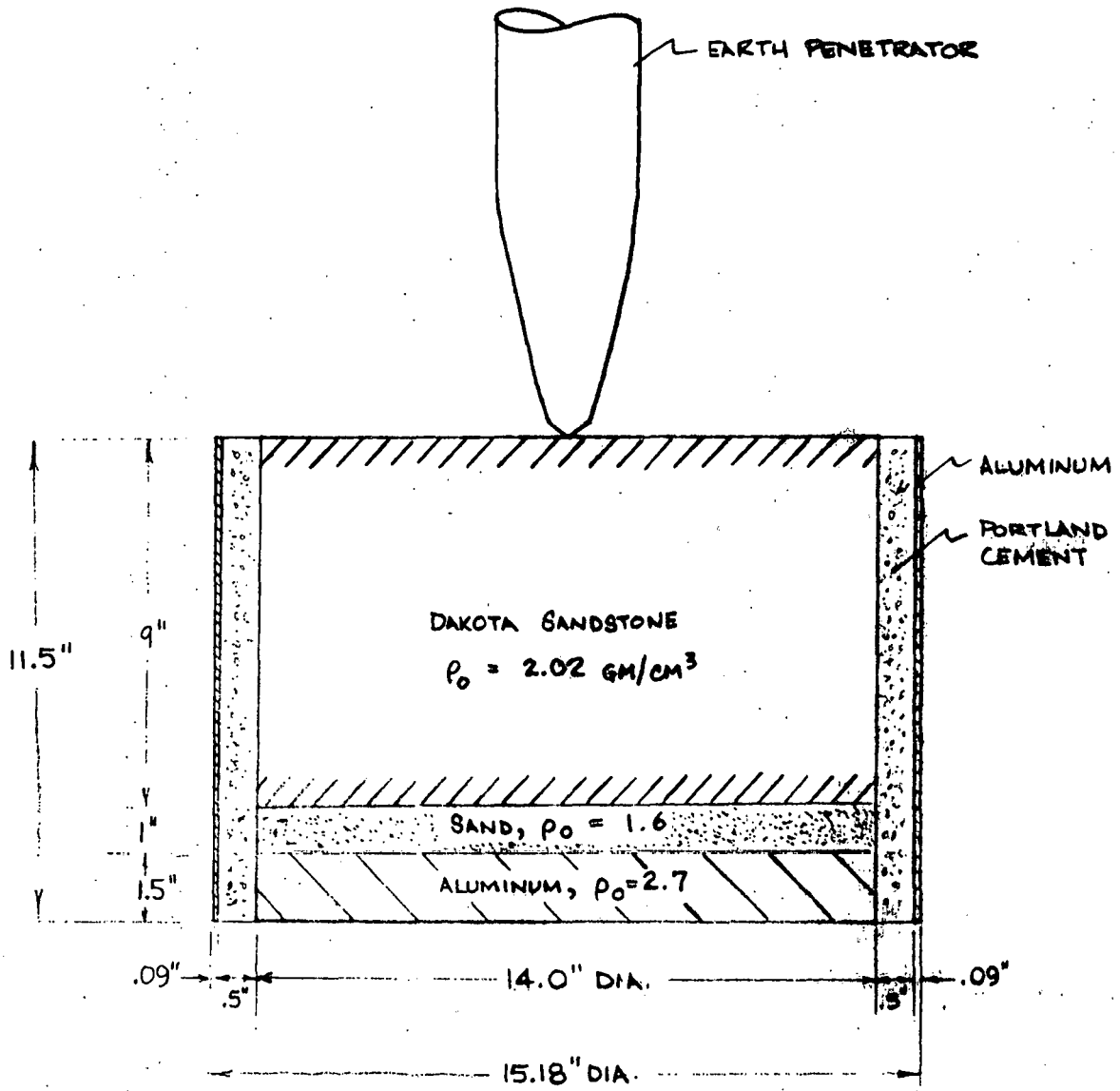

Figure 2. Layered cylinder target.

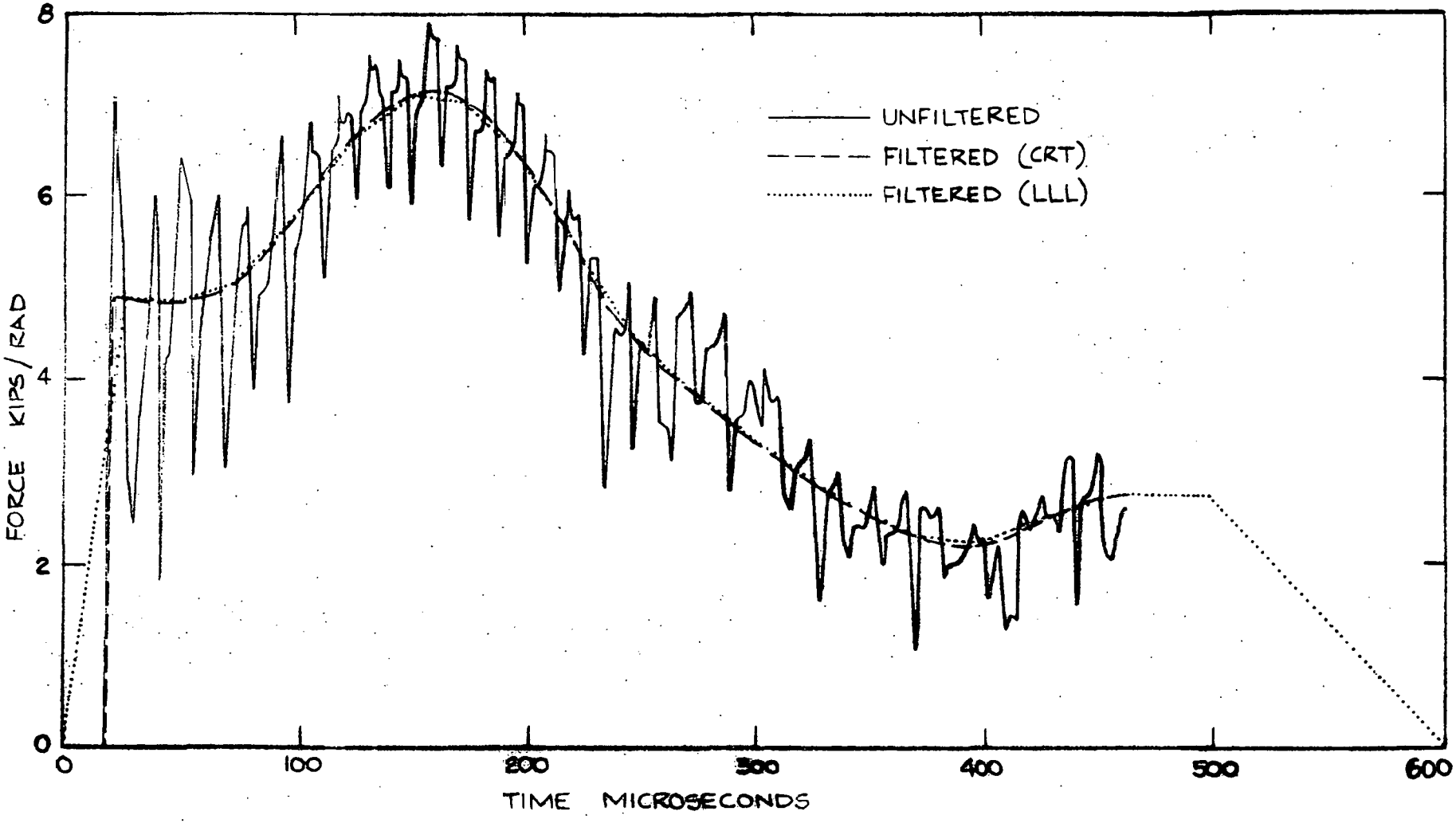

Figure 3. Typical nodal force time history.

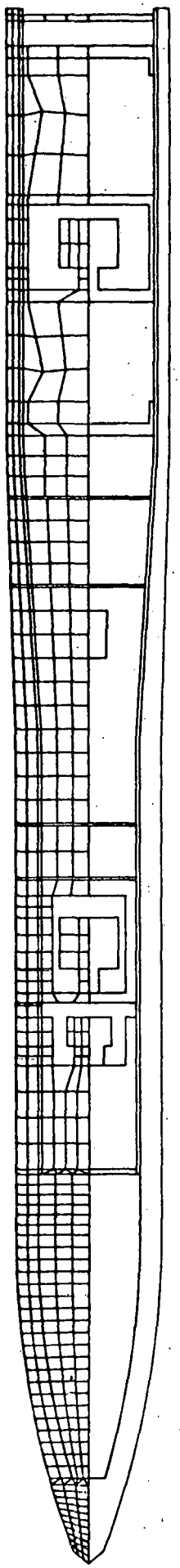

Figure 4.

Computer model of earth penetrator.

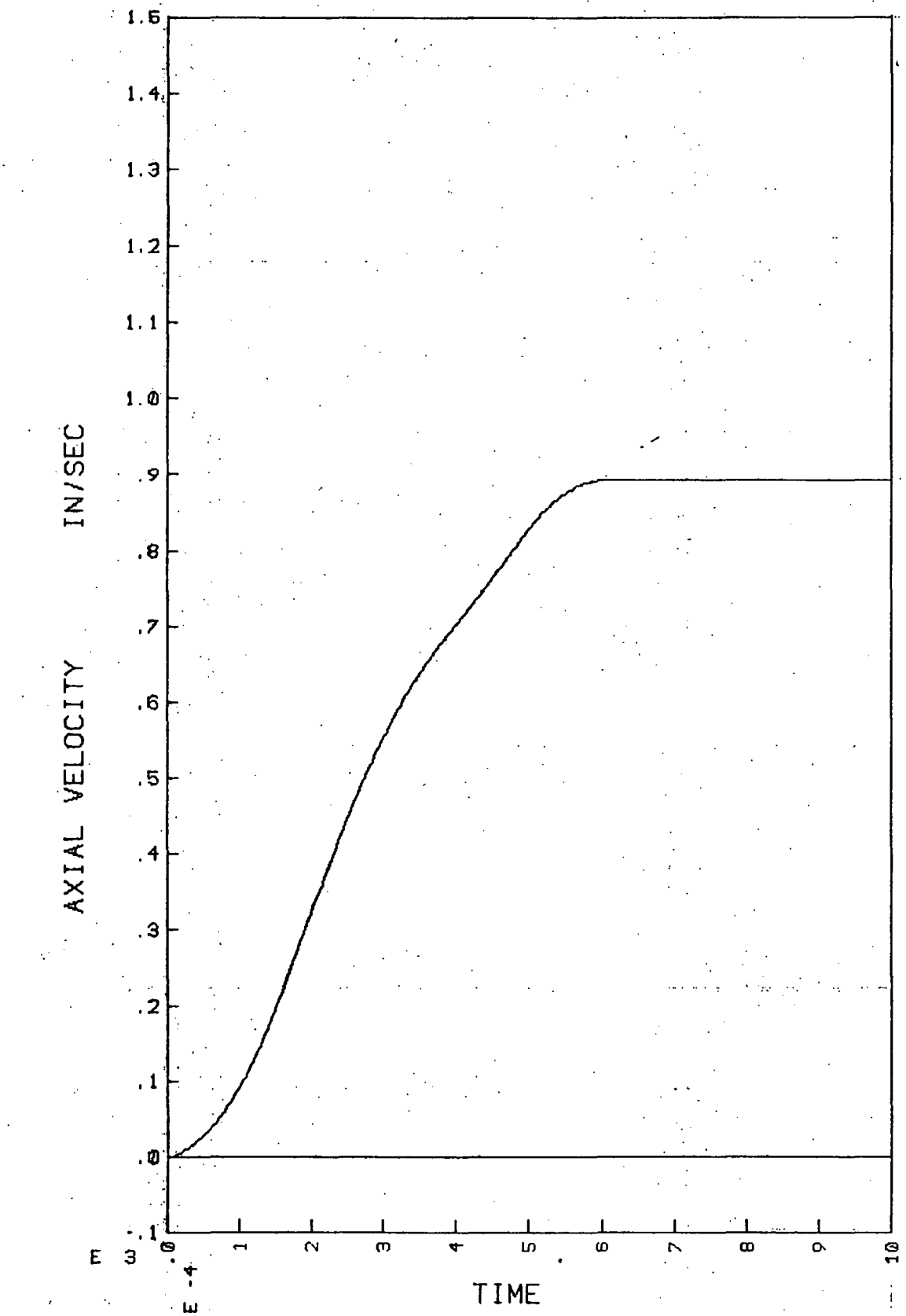

Fig. 5. Rigid body velocity.

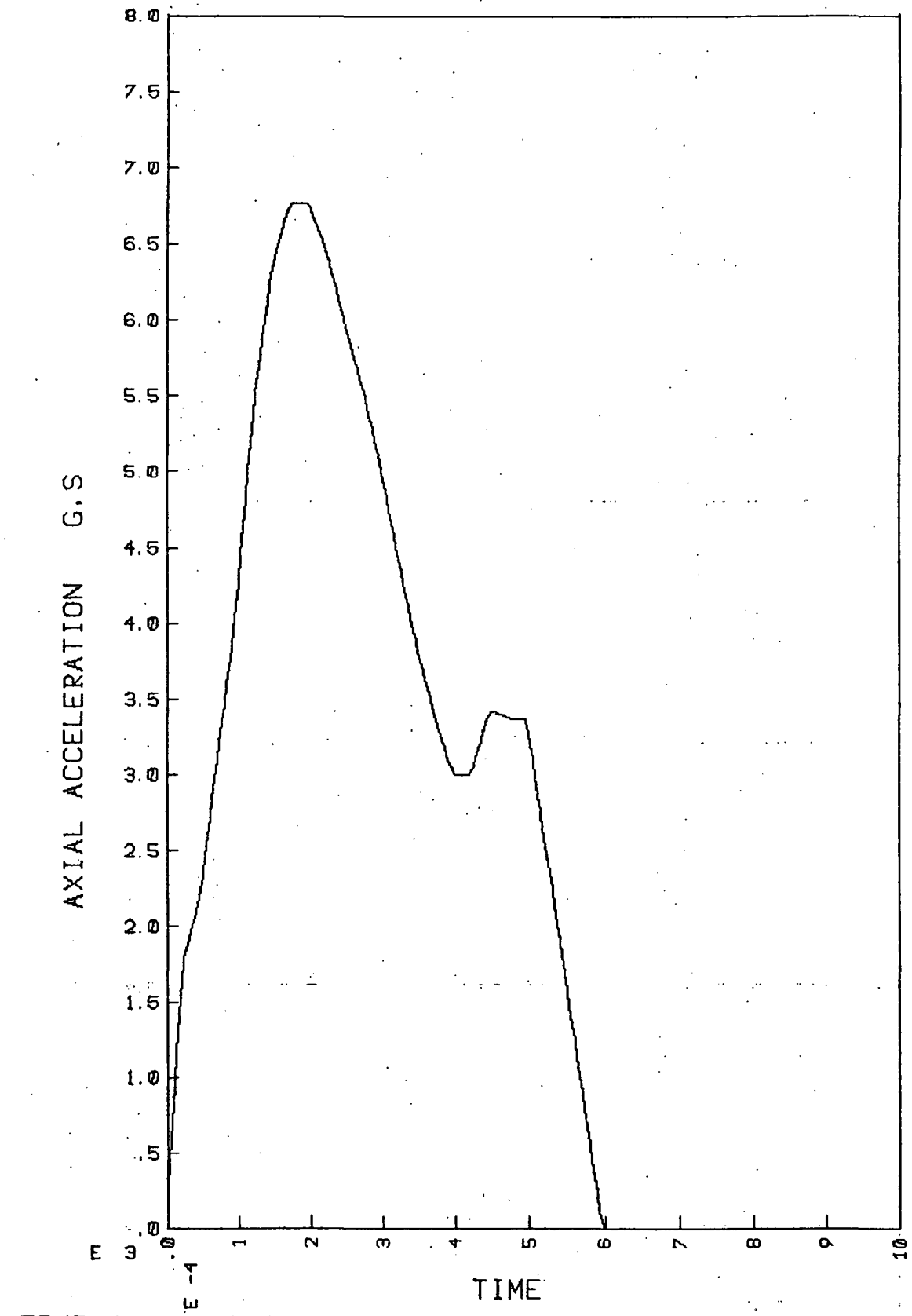

Fig. 6. Rigid body acceleration.

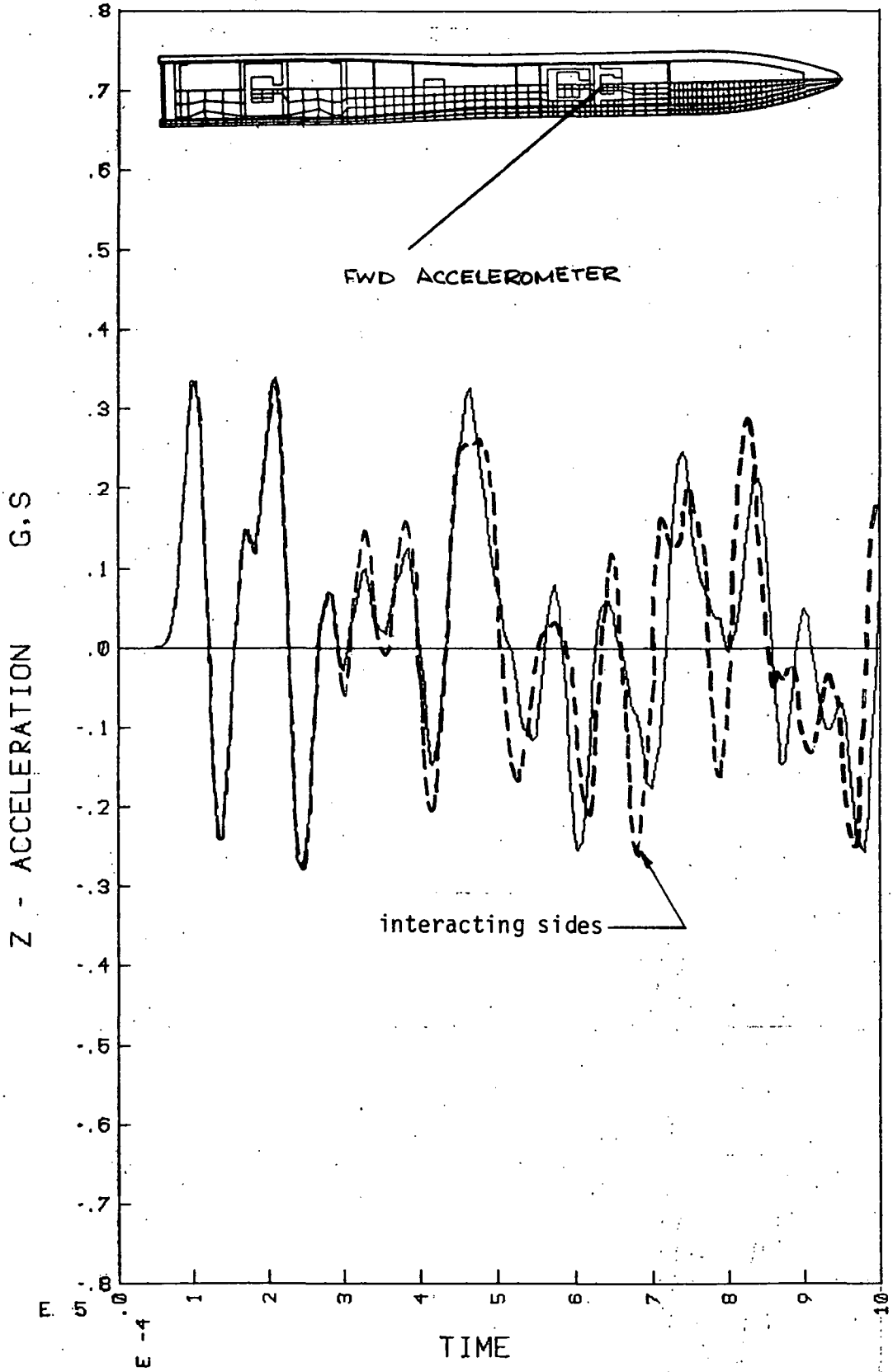

Fig. 7. Acceleration history of forward accelerometer.

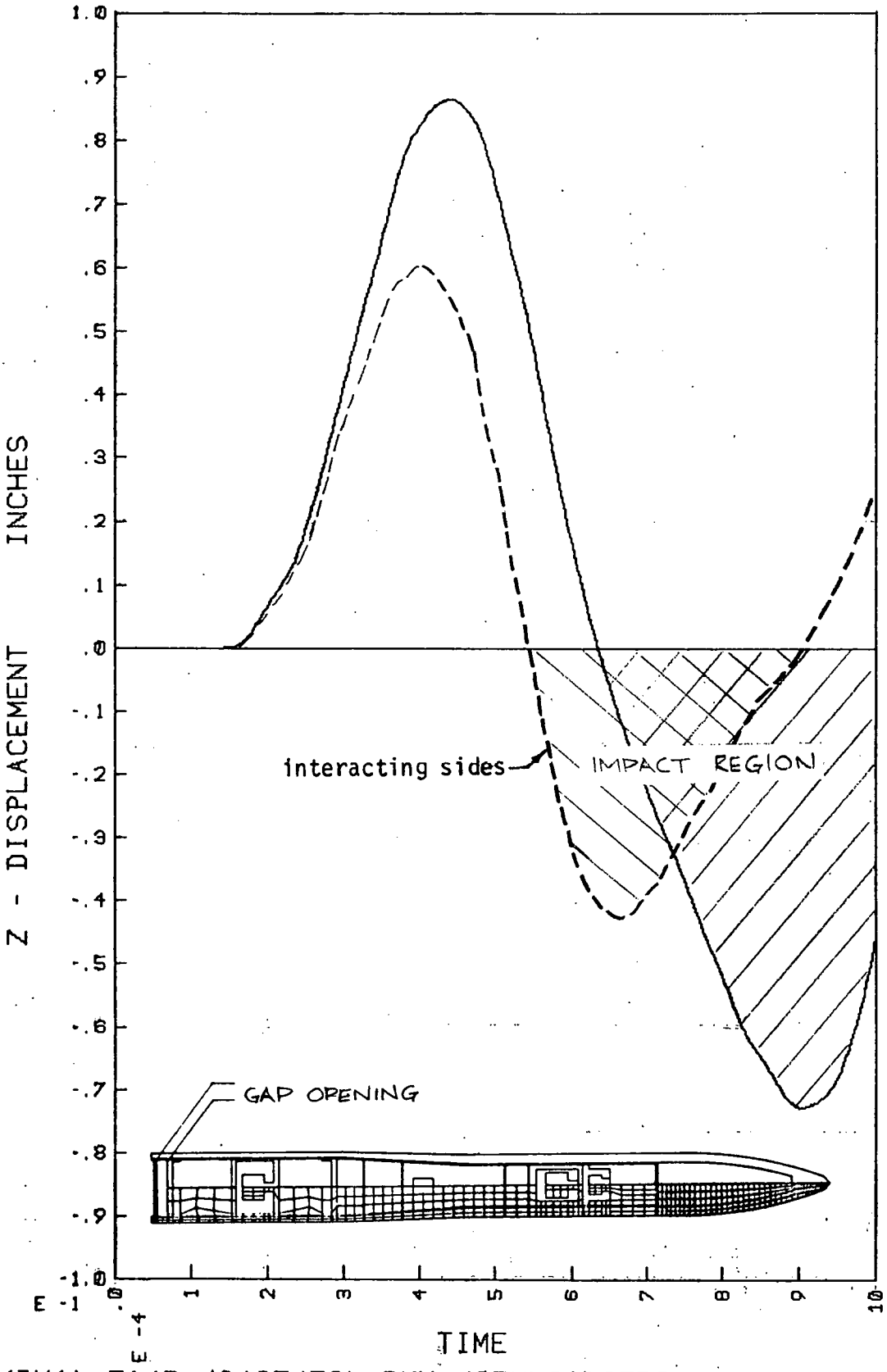

Fig. 8. Separation of liner and rear cap.

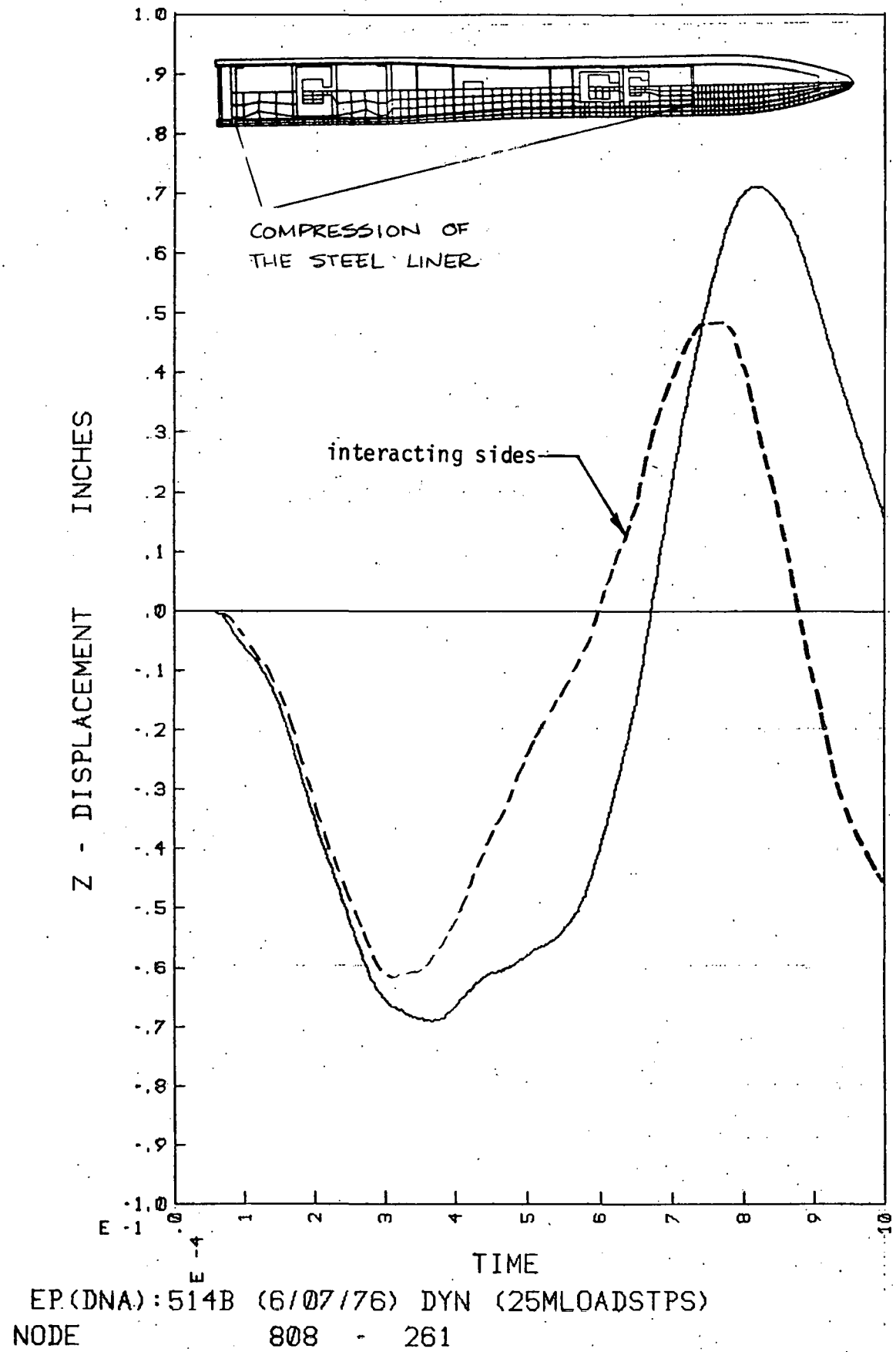

Fig. 9. Overall compression of steel liner.

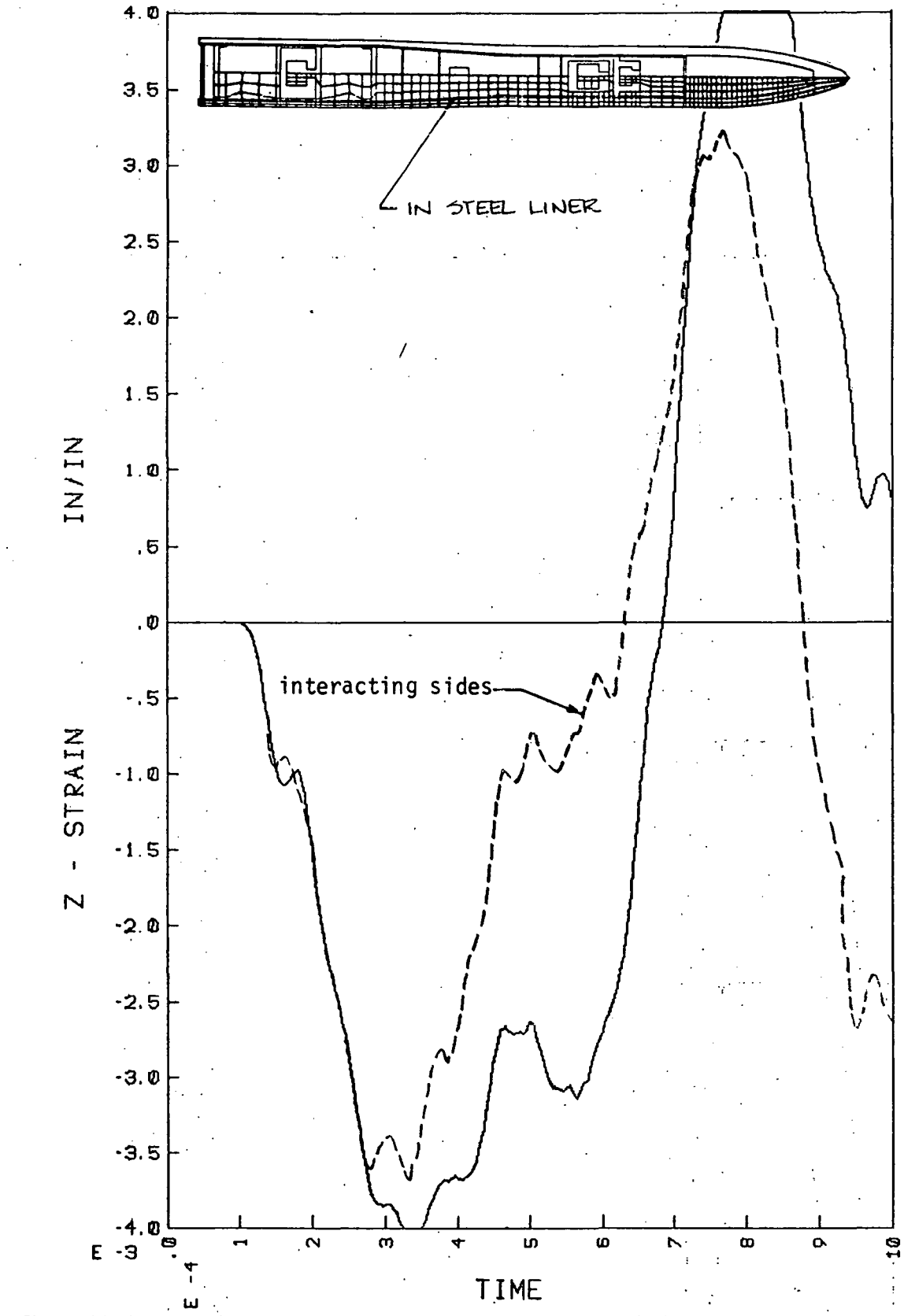

Fig. 10. Axial strain in steel liner at Station 19.50.

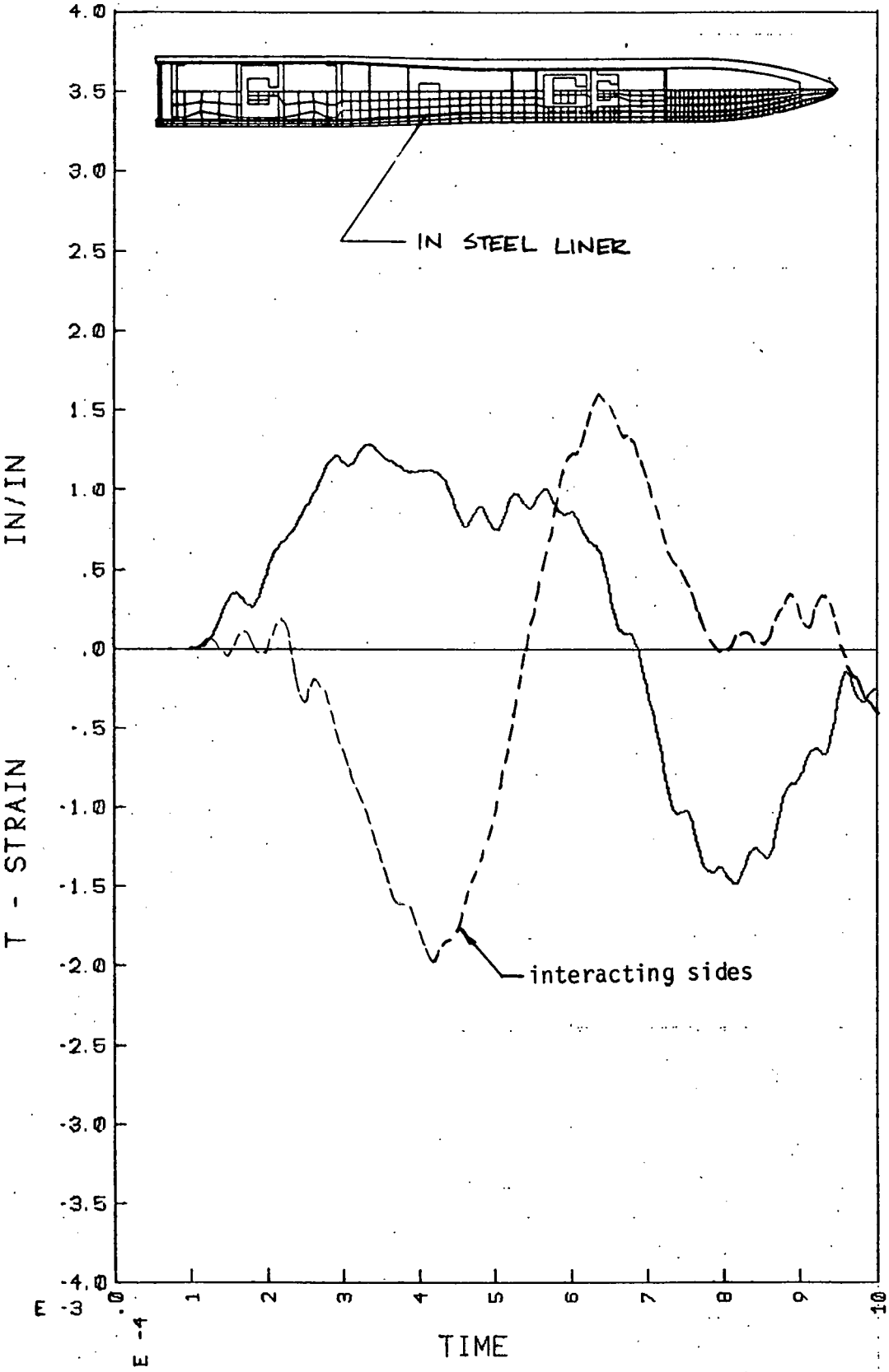

Fig. 11. Hoop strain in steel liner at Station 19.50.

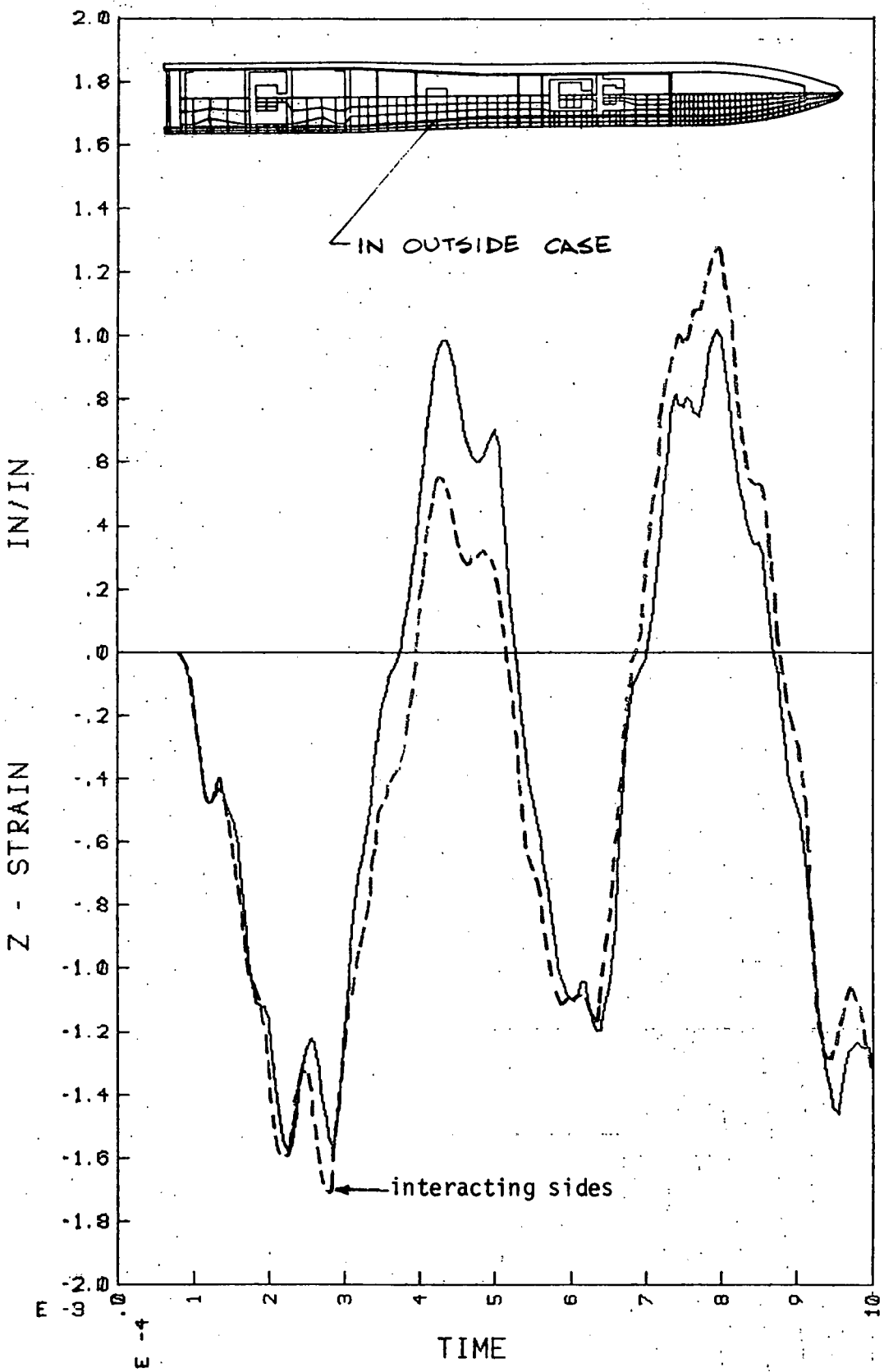

Fig. 12. Axial strain in steel case at Station 19.50.

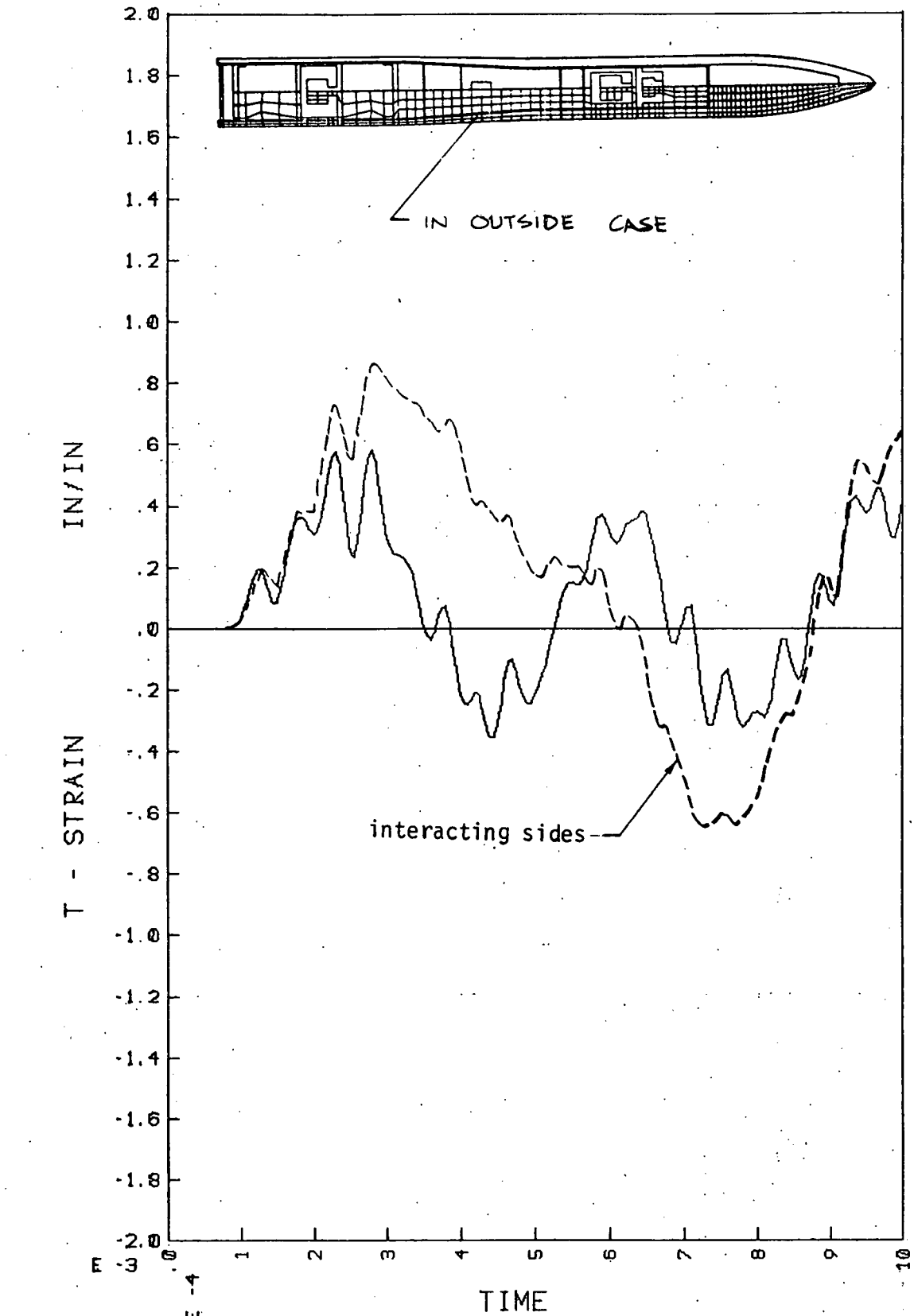

Fig. 13. Hoop strain in steel case at Station 19.50.

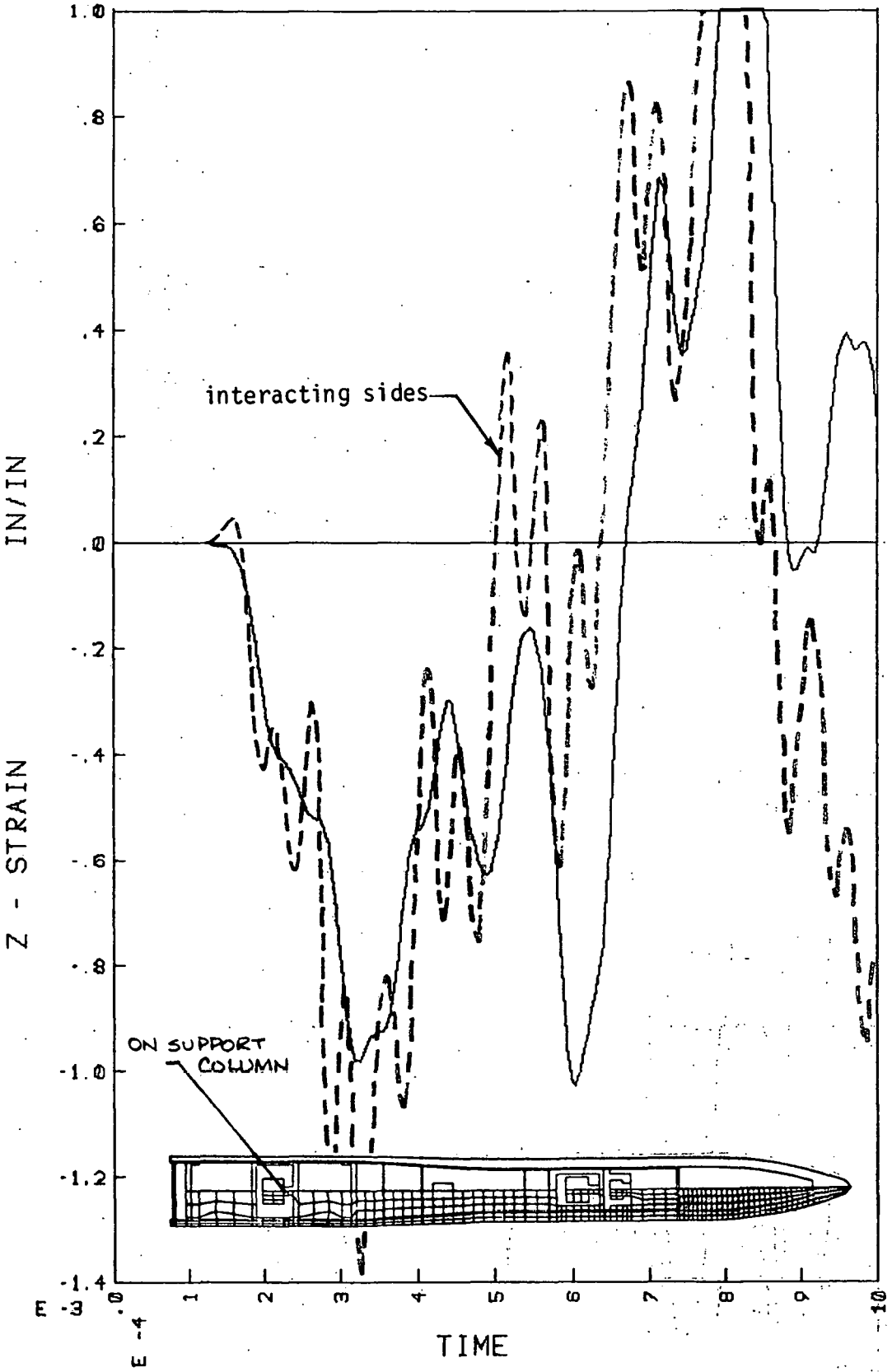

Fig. 14. Axial strain on support column at Station 26.50.

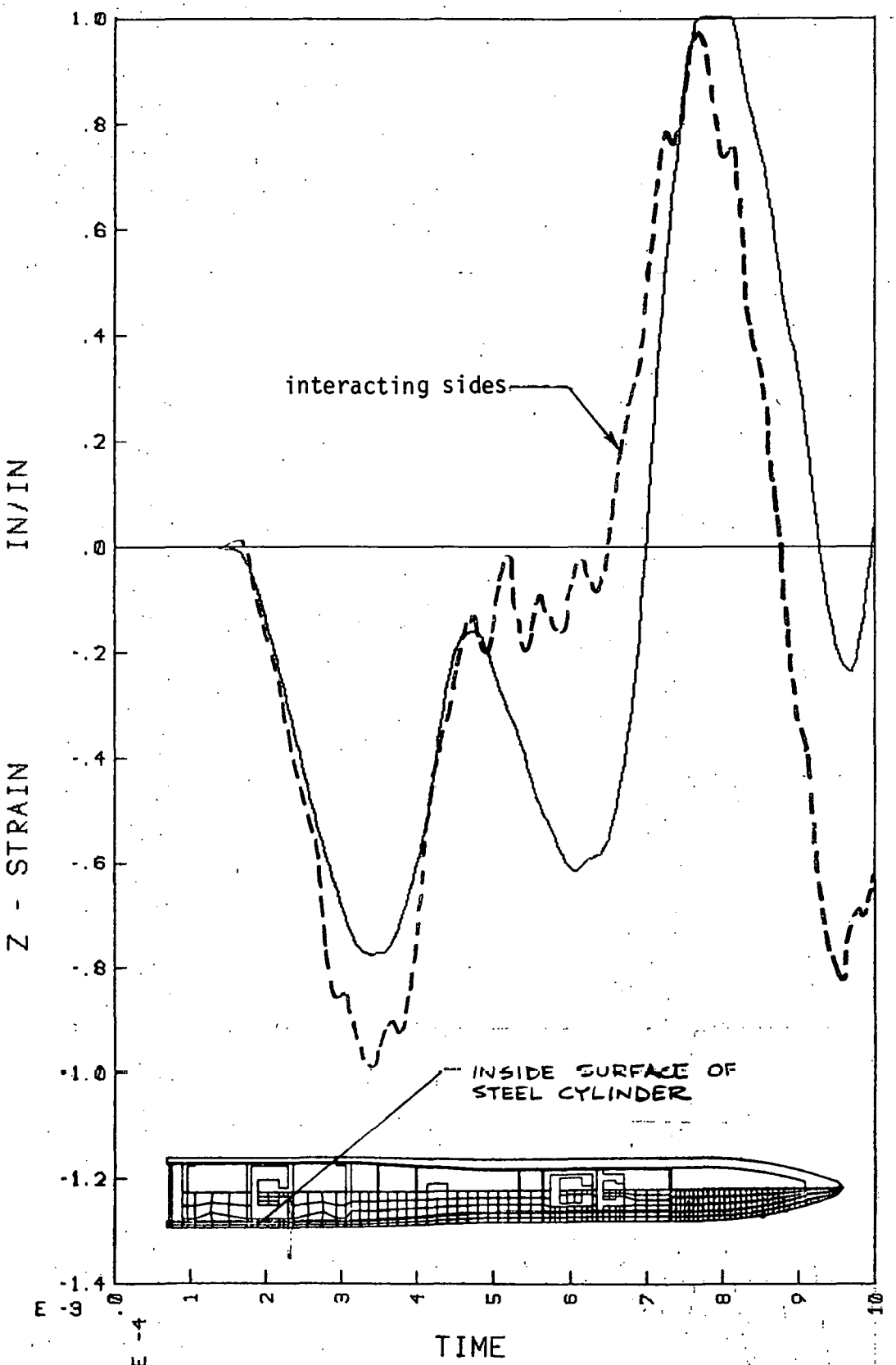

Fig. 15. Axial strain in steel liner at Station 27.30.

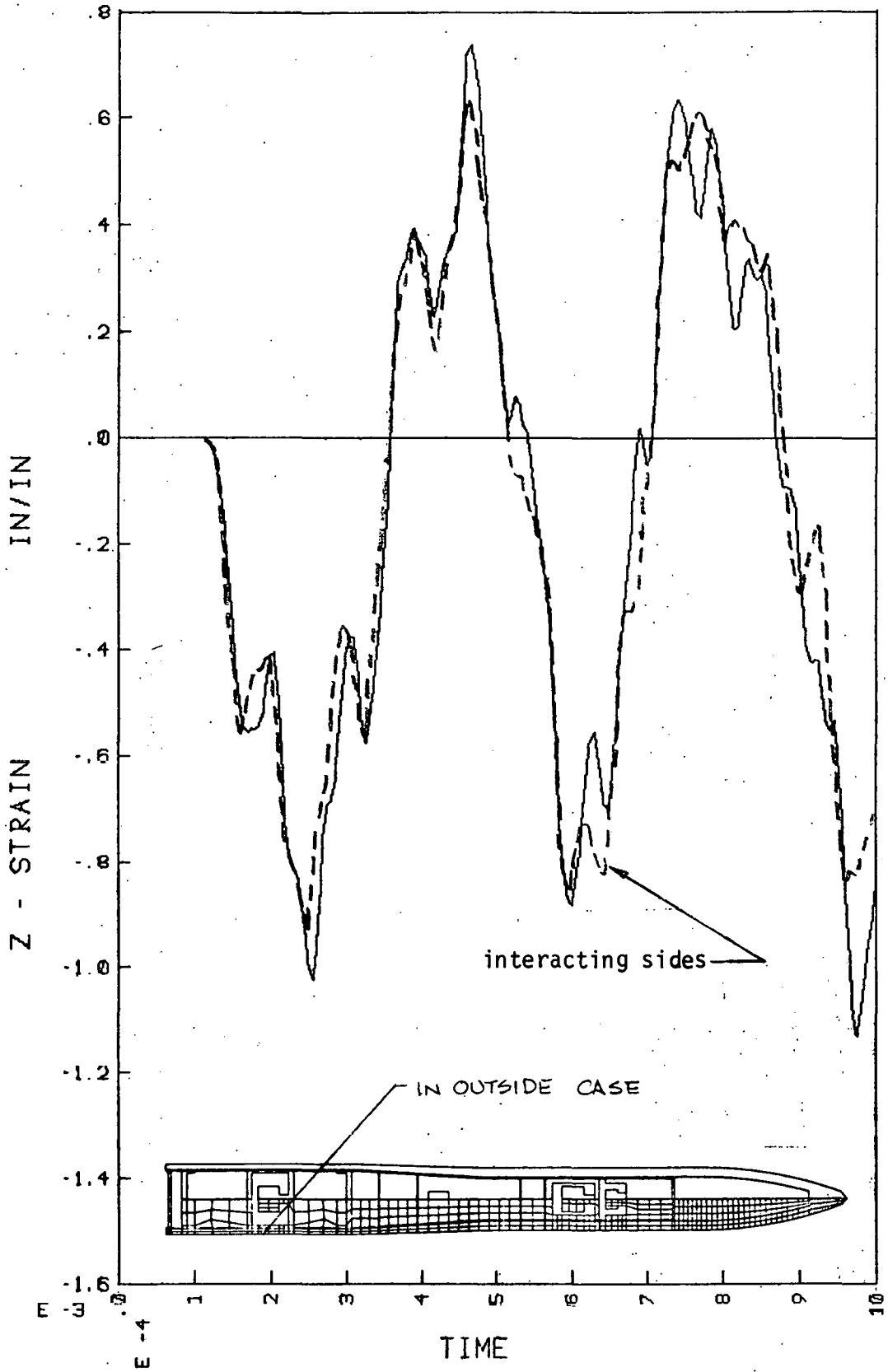

Fig. 16. Axial strain in steel case at Station 27.30.

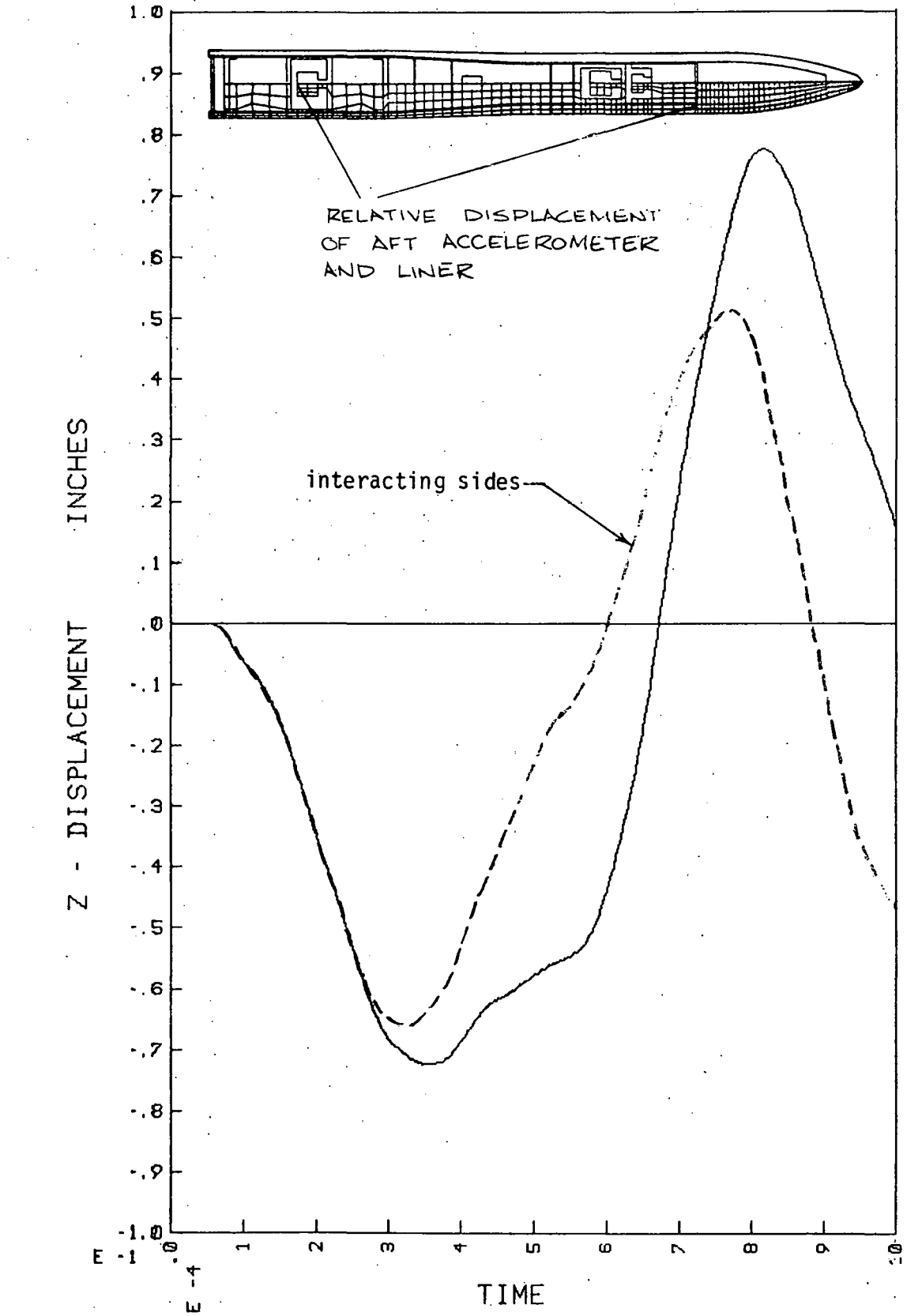

Fig. 17. Relative displacement of aft accelerometer and liner.

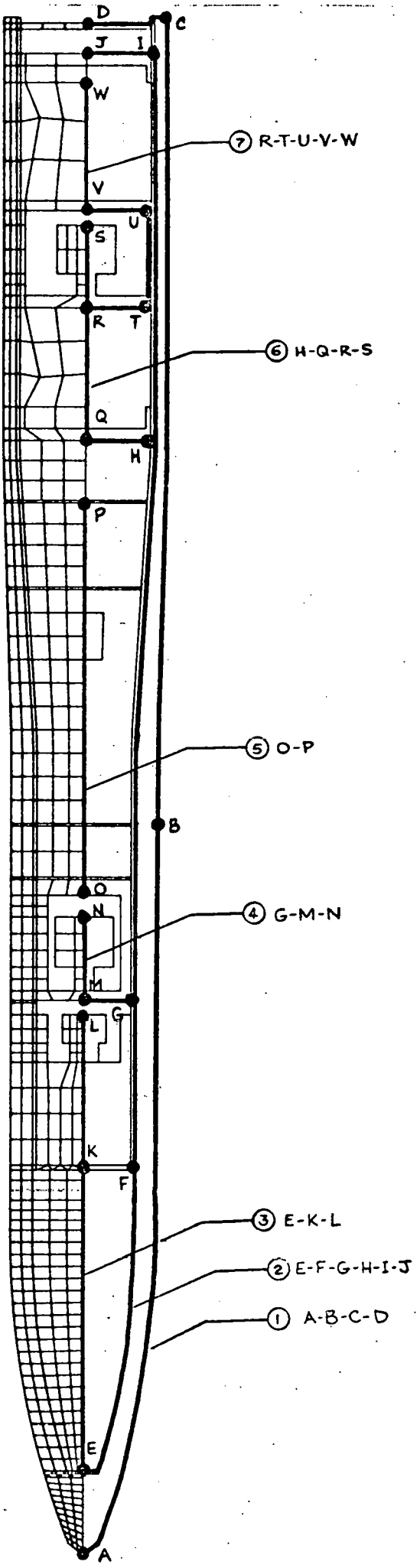

Figure 18. Nodal path for mode shape analysis.

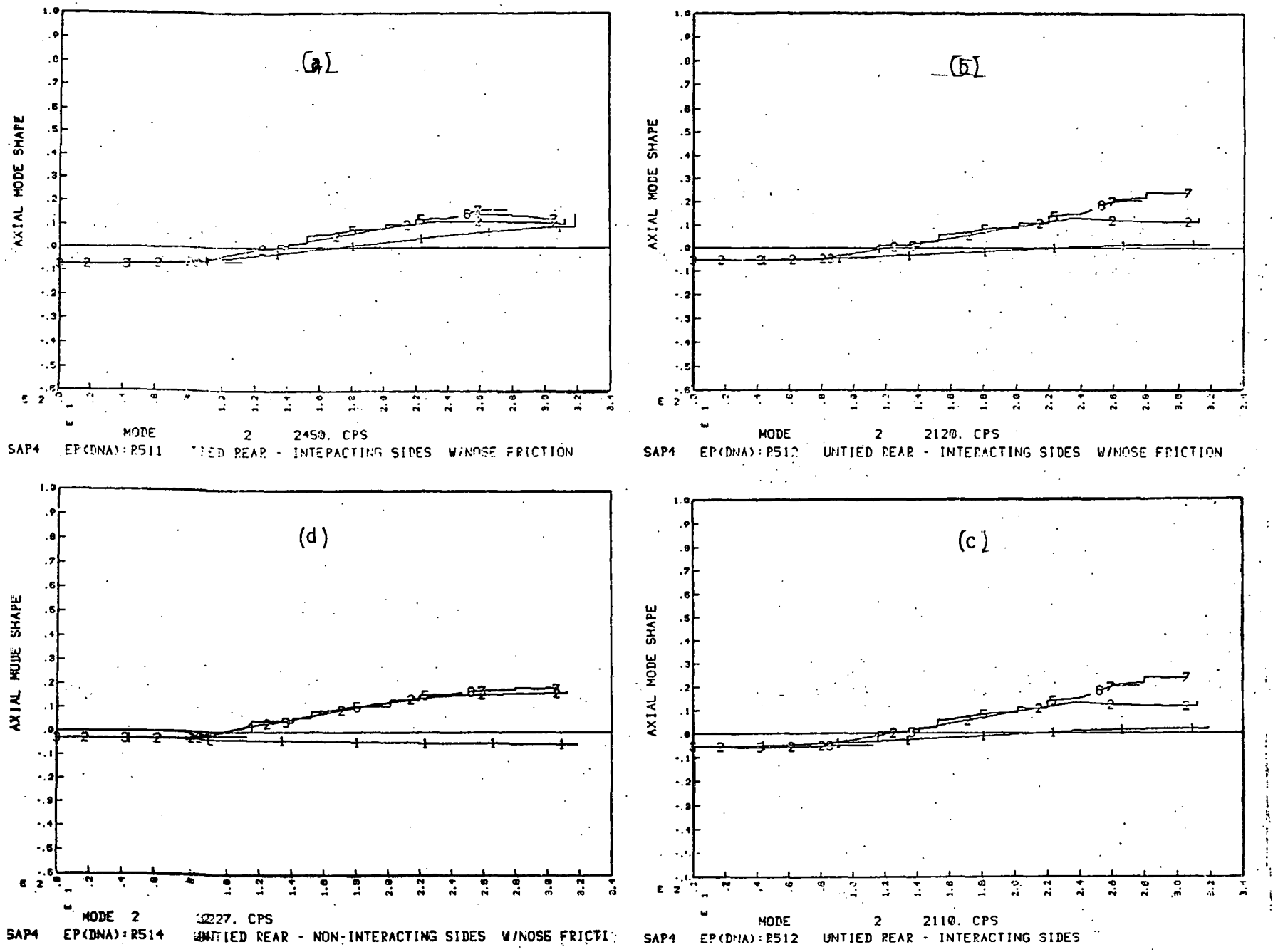

Fig. 19. Mode shape vs. axial station for Mode 2.

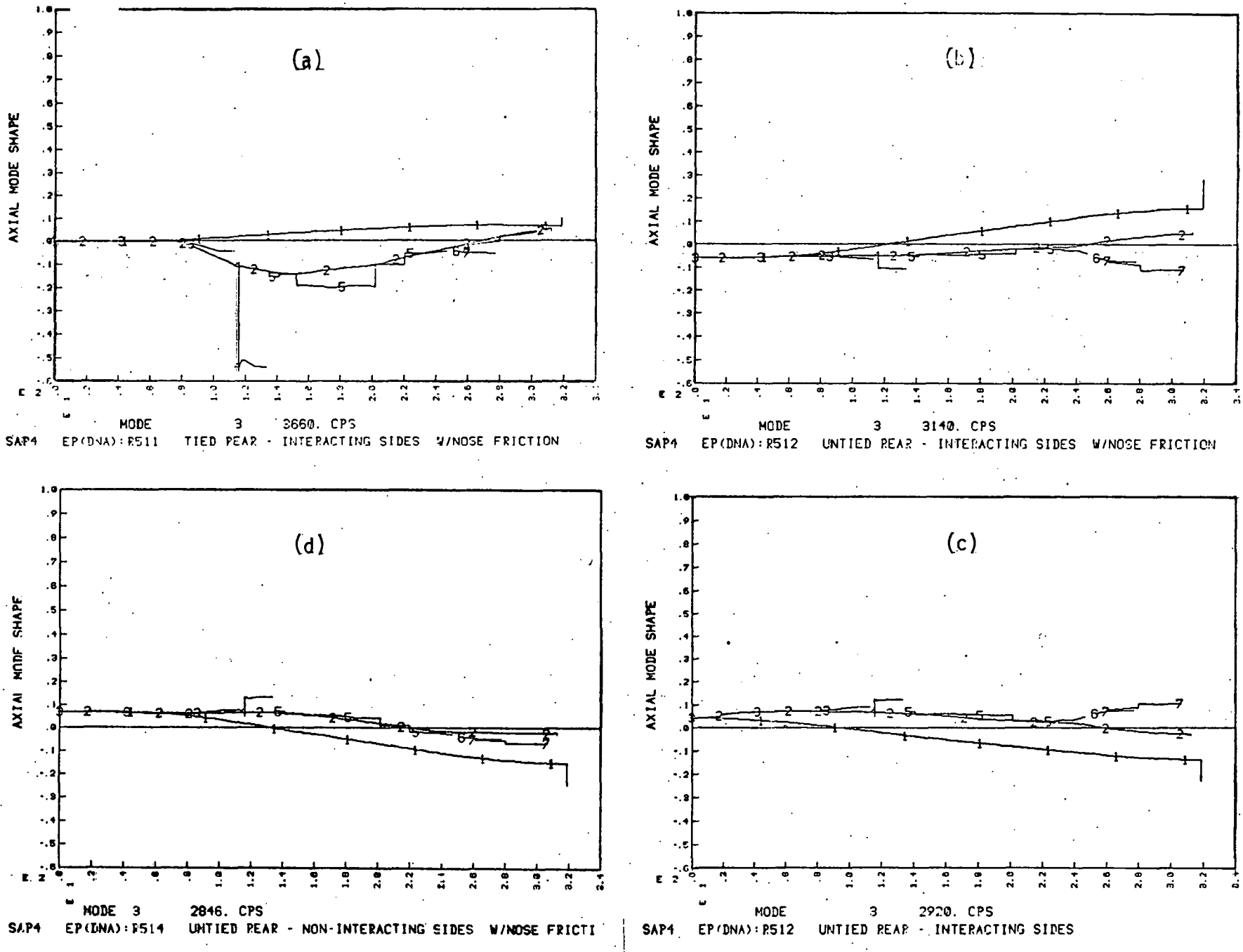

Fig. 20. Mode shape vs.axial station for Mode 3.

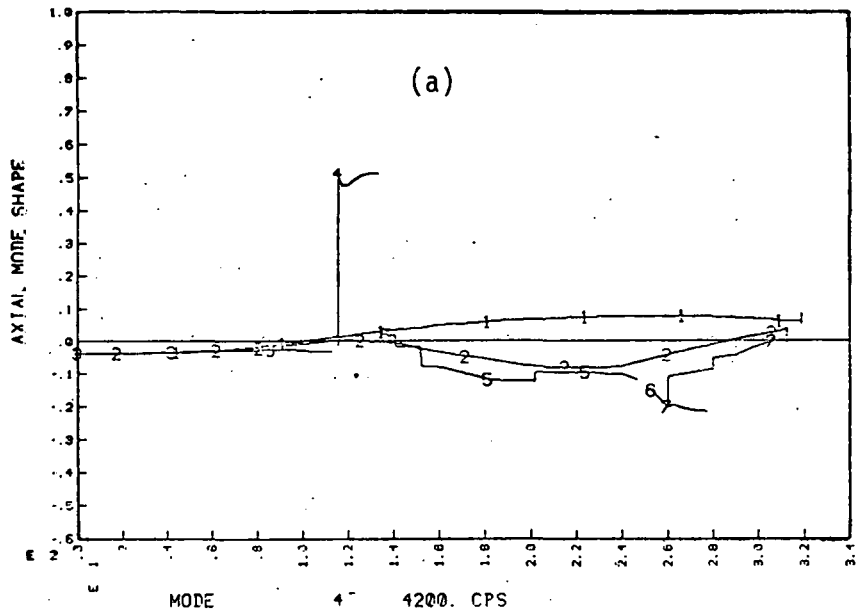

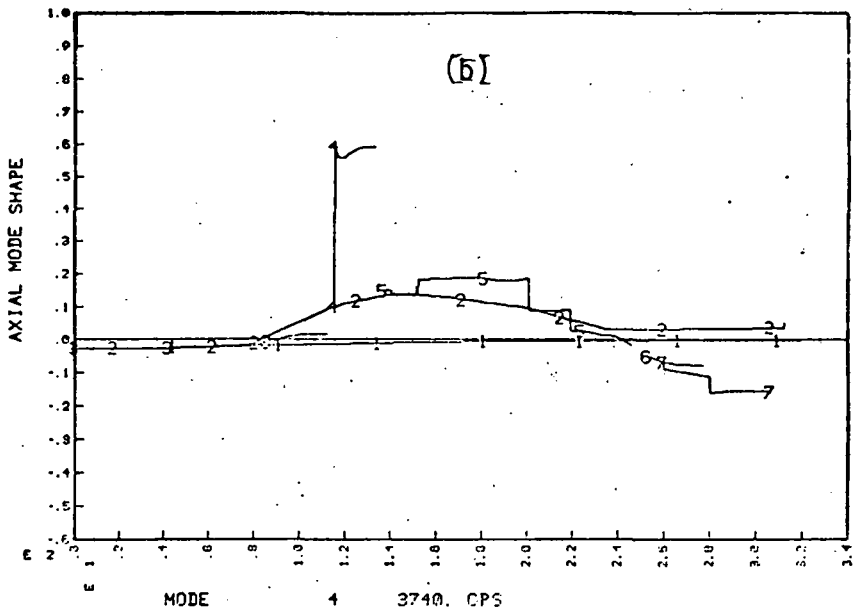

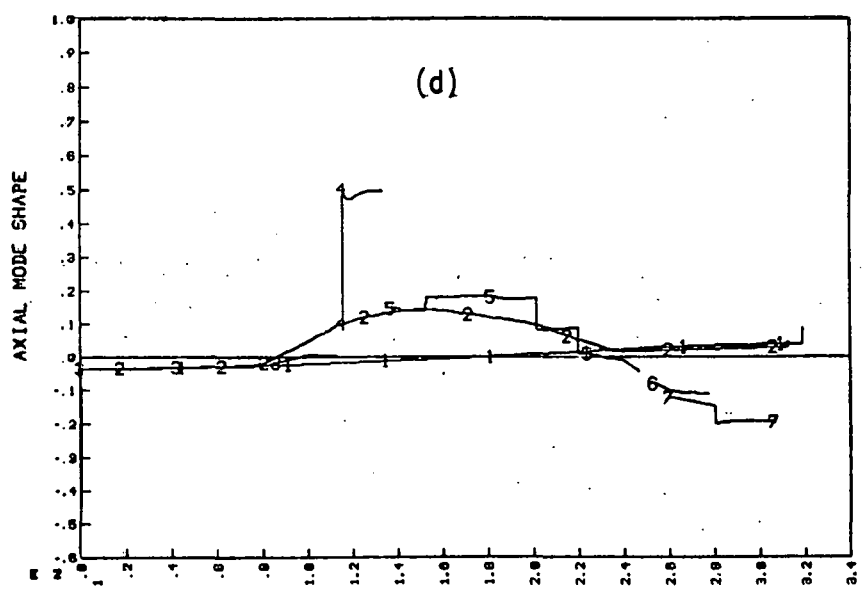

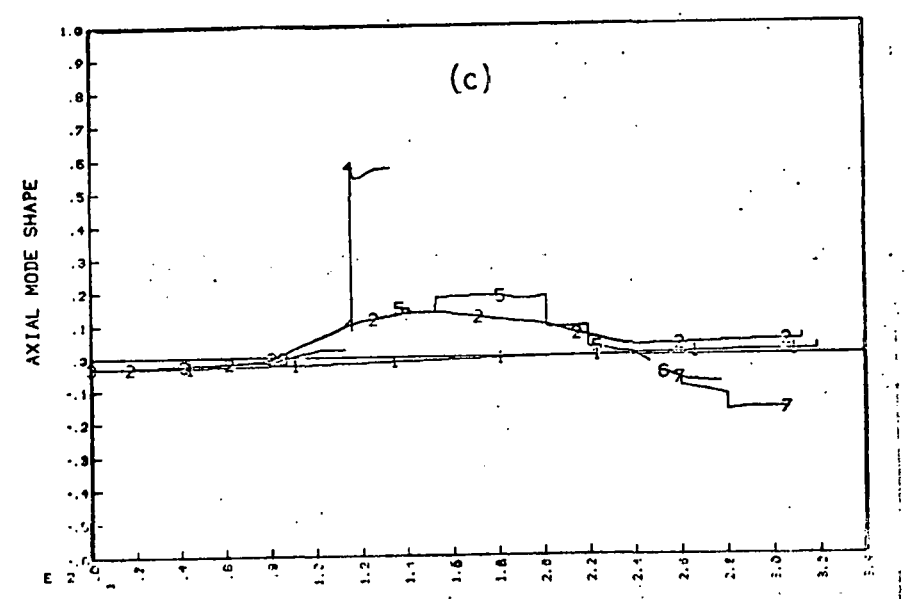

Fig. 20. Mode shape vs.axial station for Mode 4.

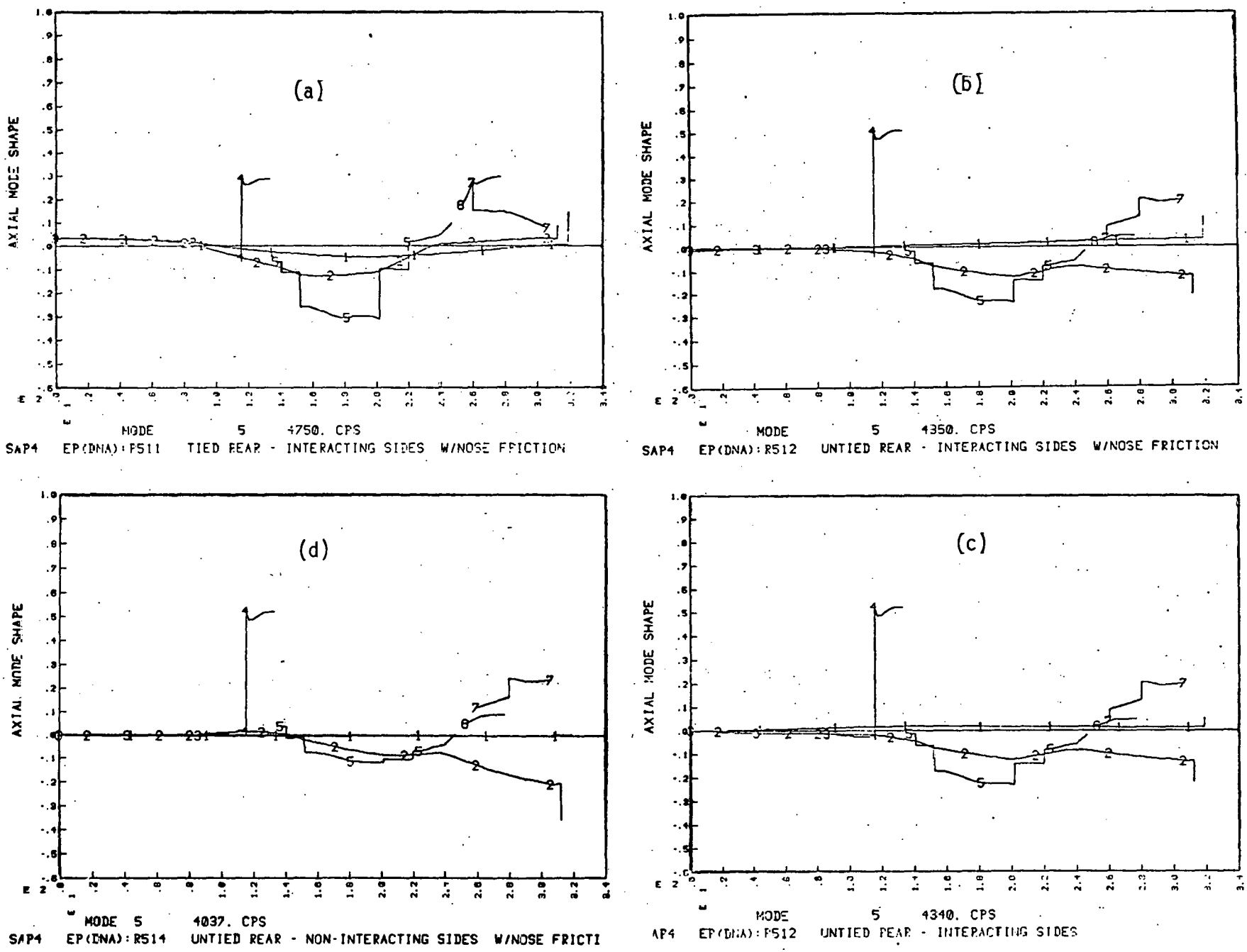

Fig. 22. Mode shape vs. axial station for Mode 5.

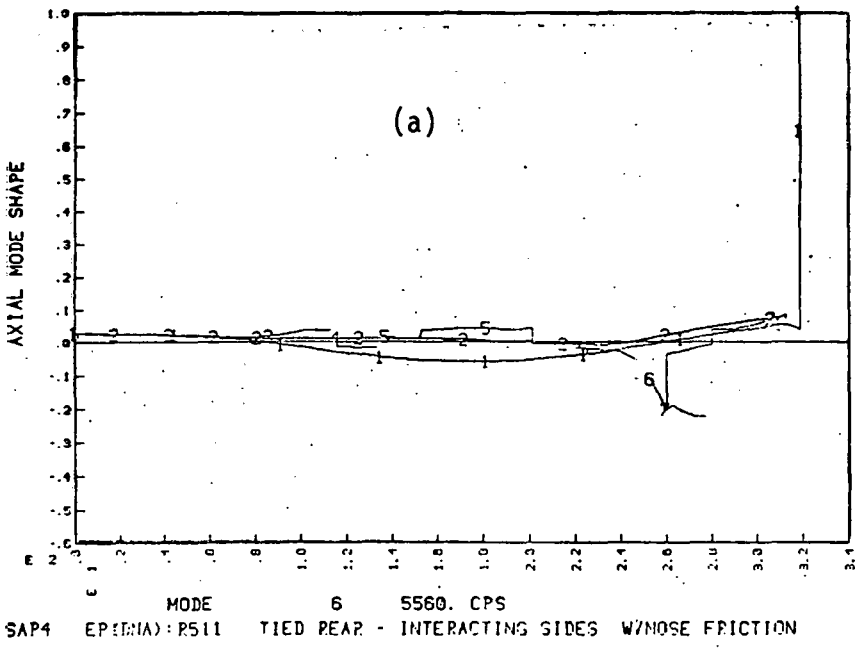

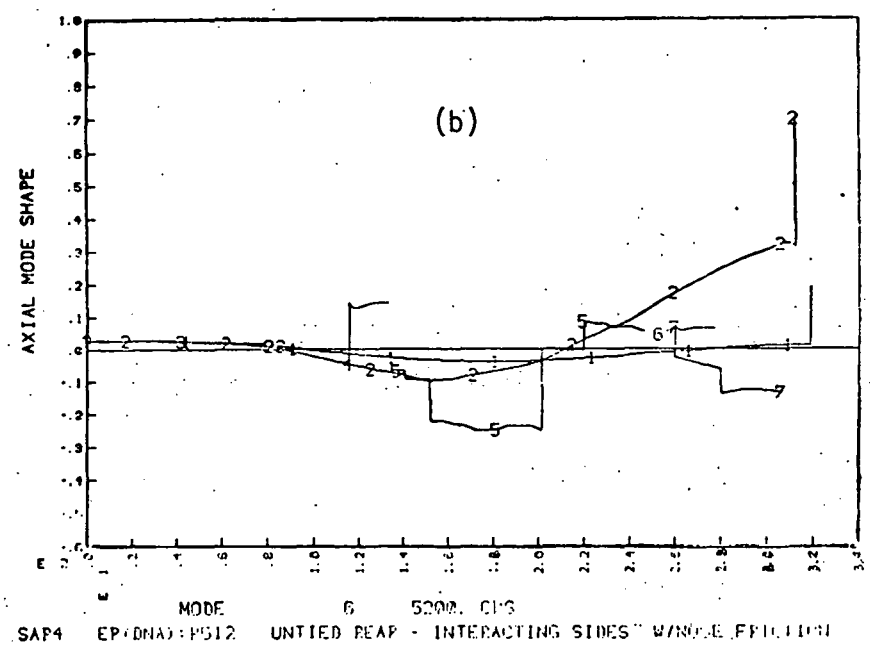

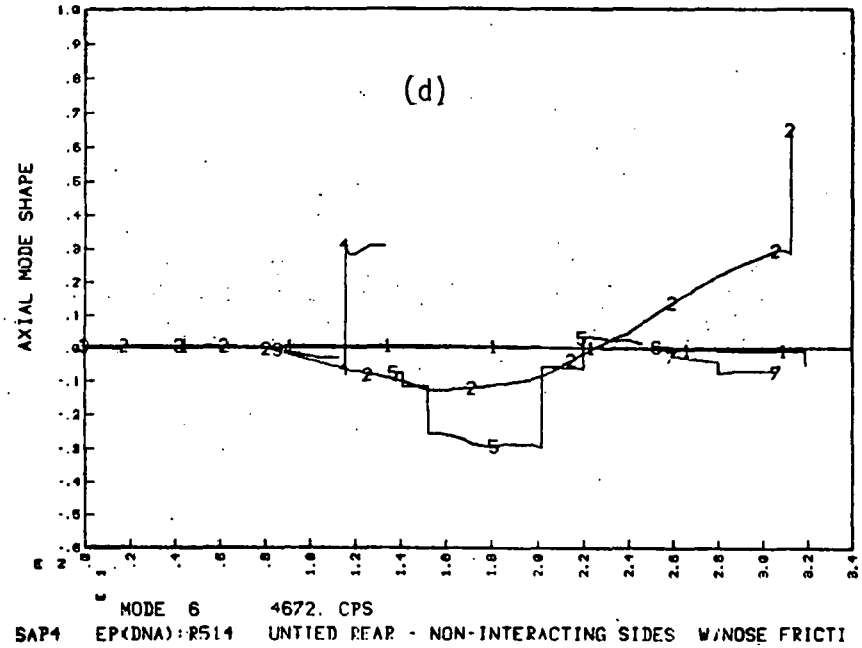

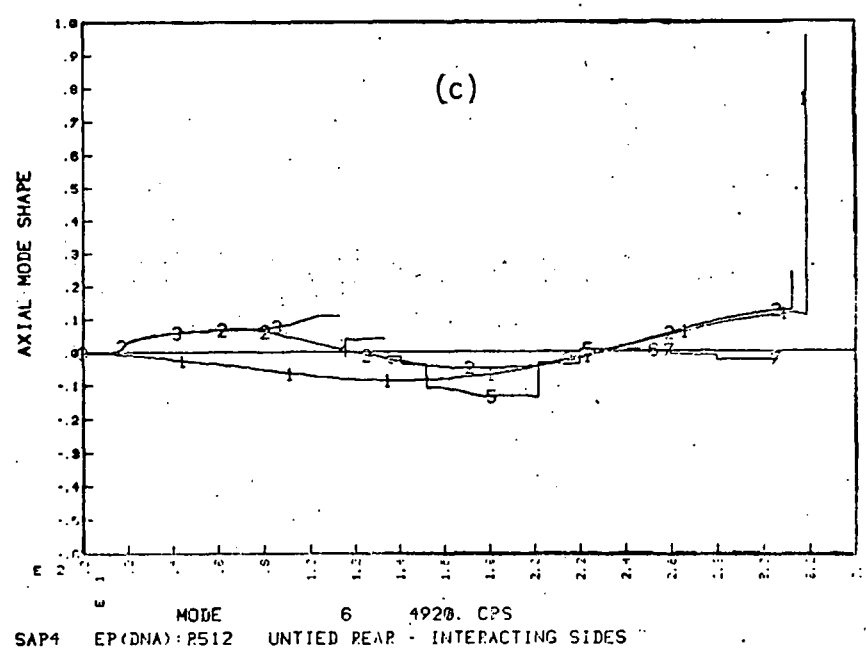

Fig. 23. Mode shape vs. axial station for Mode. 6.

APPENDIX

This appendix includes time histories for the first 500 microseconds and multipoints of component distories for 500 and 1000 microseconds for easy comparison.

FIGURES

B6. Axial stresses at same locations.

B7. Axial stress distribution at rear interface of ballast.

C1. Axial velocities of principal structure stations.

C2. Axial velocities of stations along liner.

C3. Axial velocities of points in rear assembly.

C4. Axial velocities of points in front assembly.

C5. Axial strains at key locations.

C6. Axial stresses at same locations.

C7. Axial stress distribution at rear interface of ballast.

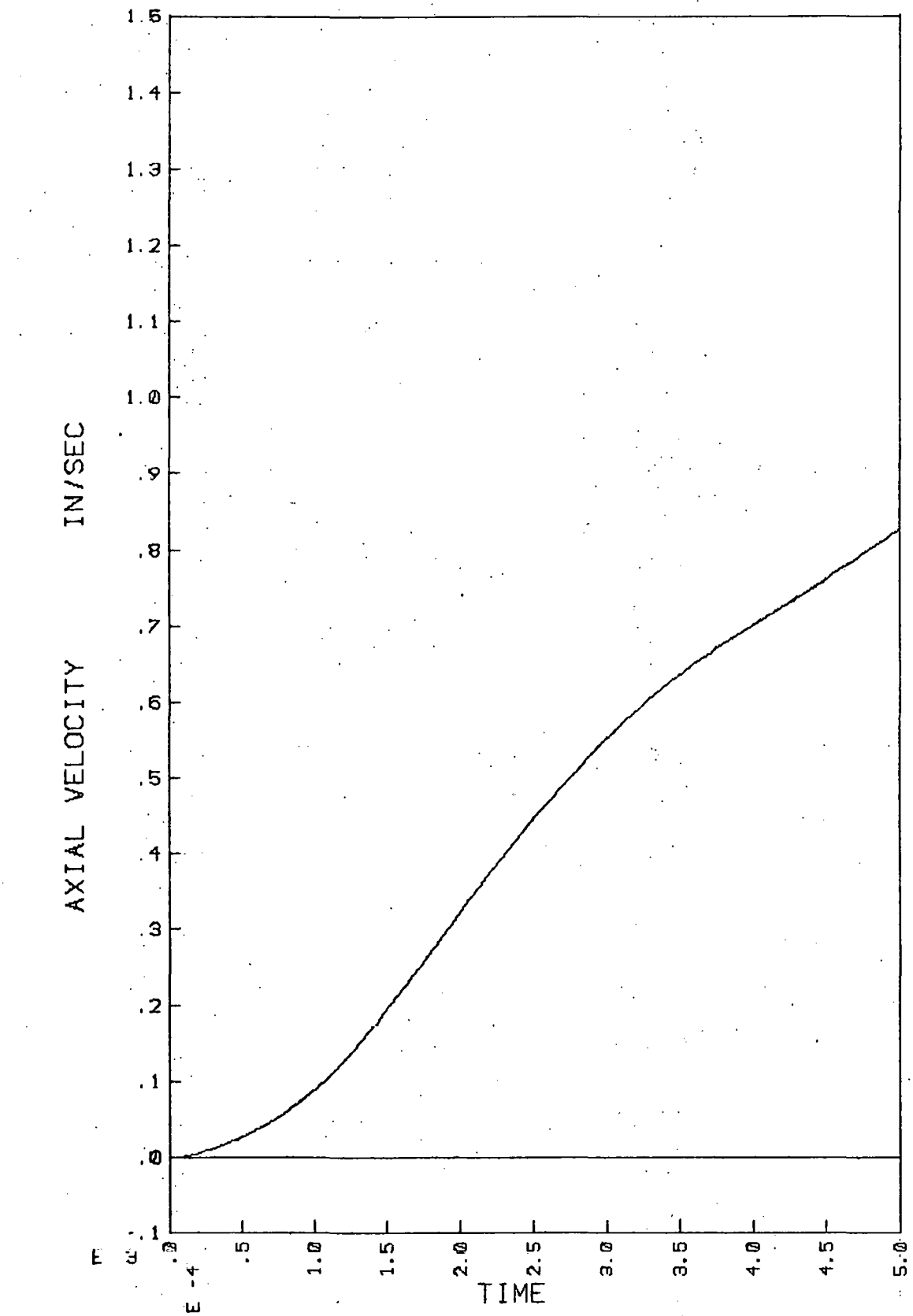

A1. Rigid body velocity.

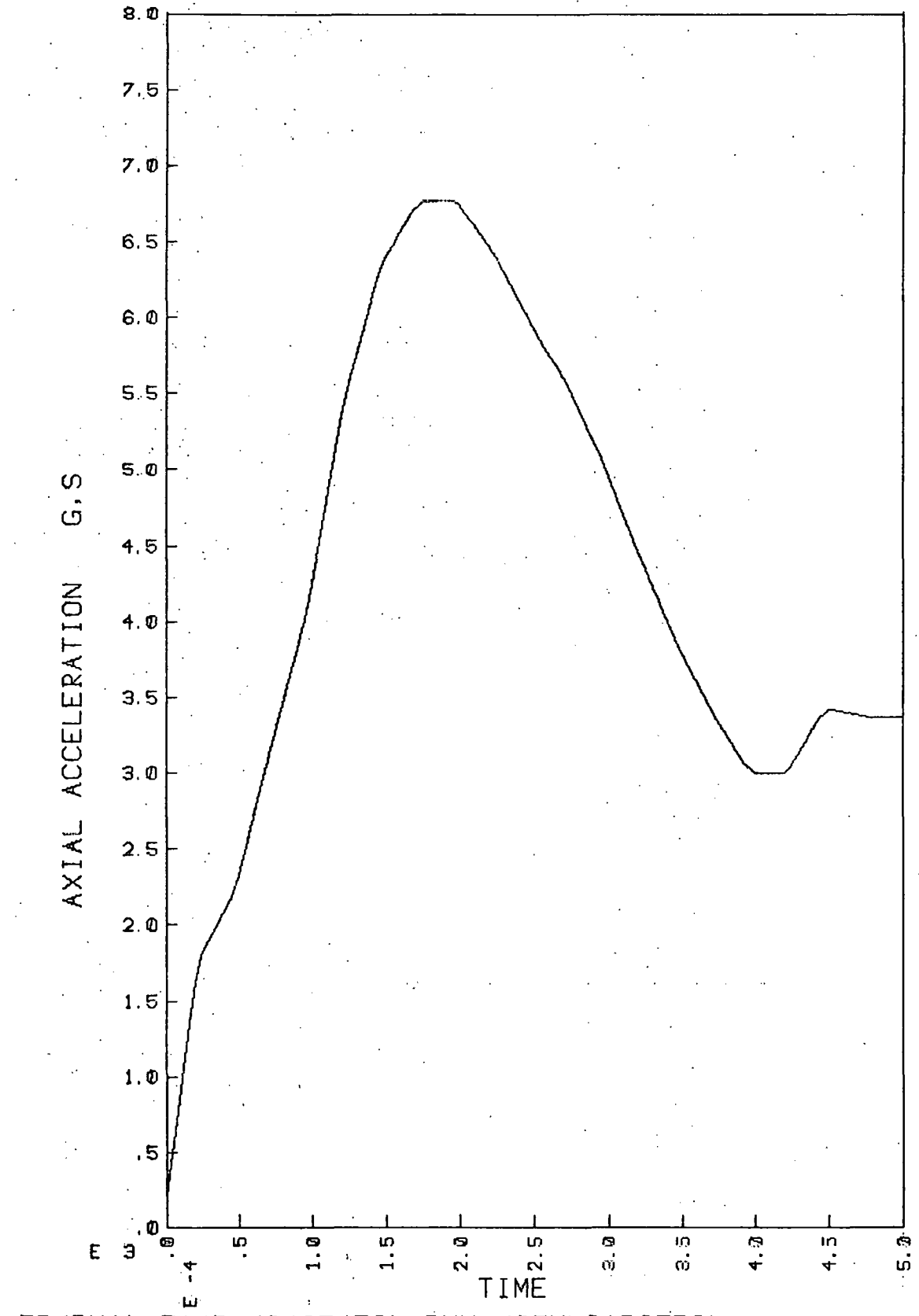

A2. Rigid body acceleration.

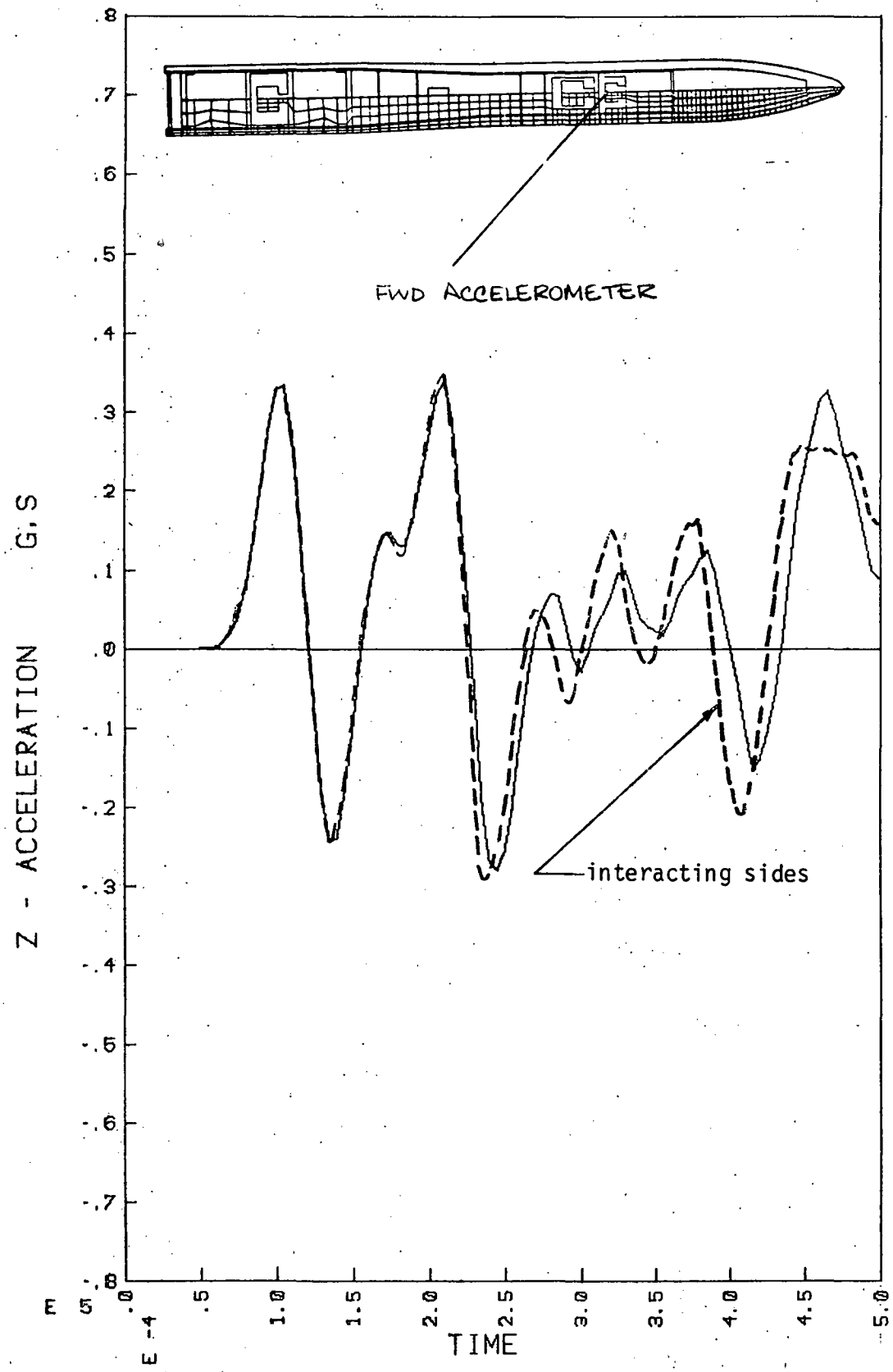

EP(DNA):514B (6/07/76) DYN (25MLOADSTPS)
NODE 338

A3. Axial acceleration of forward accelerometer.

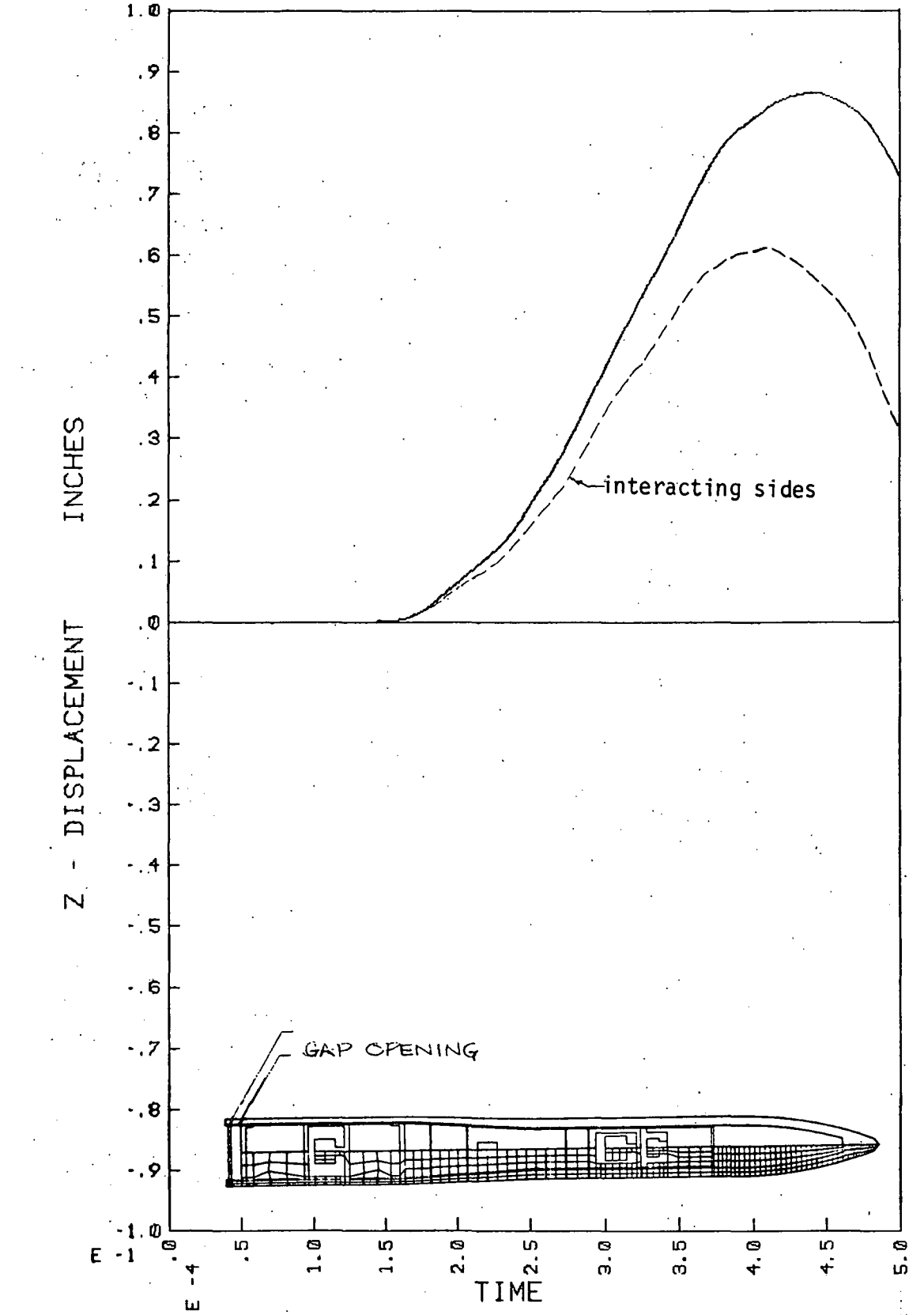

A4. Gap opening at rear plate.

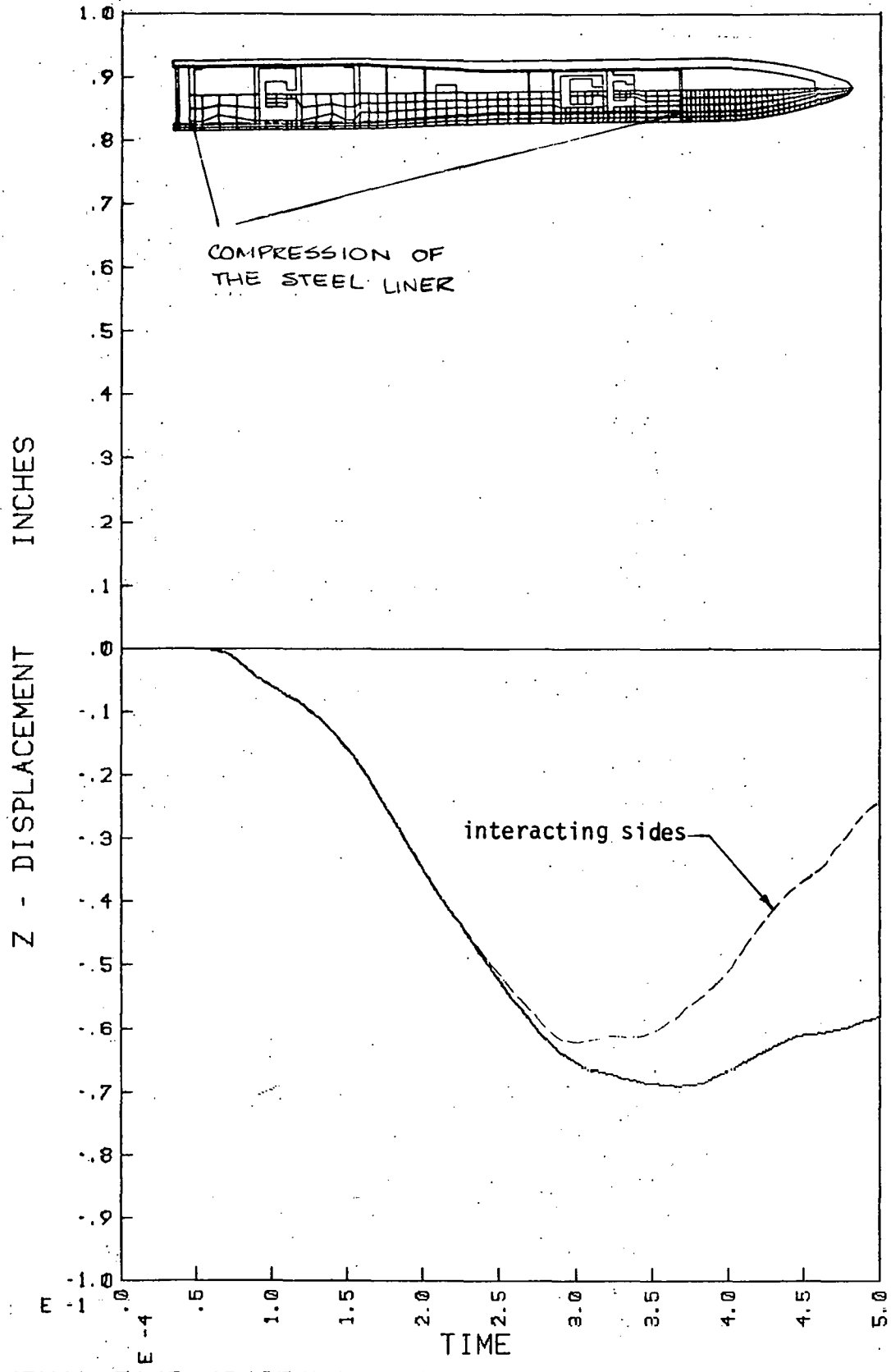

A5. Compression of steel liner.

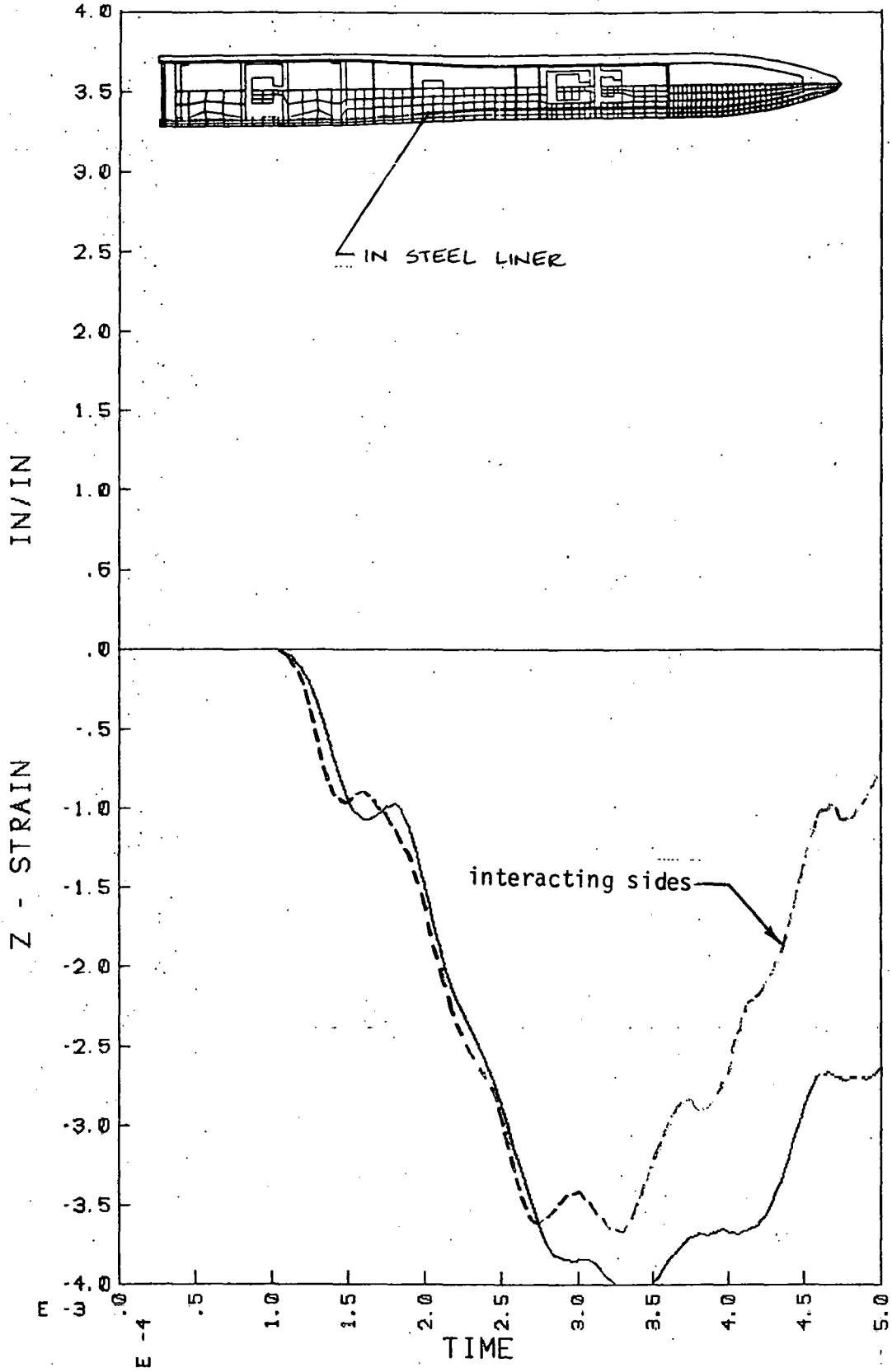

A6. Axial strain in liner at taper.

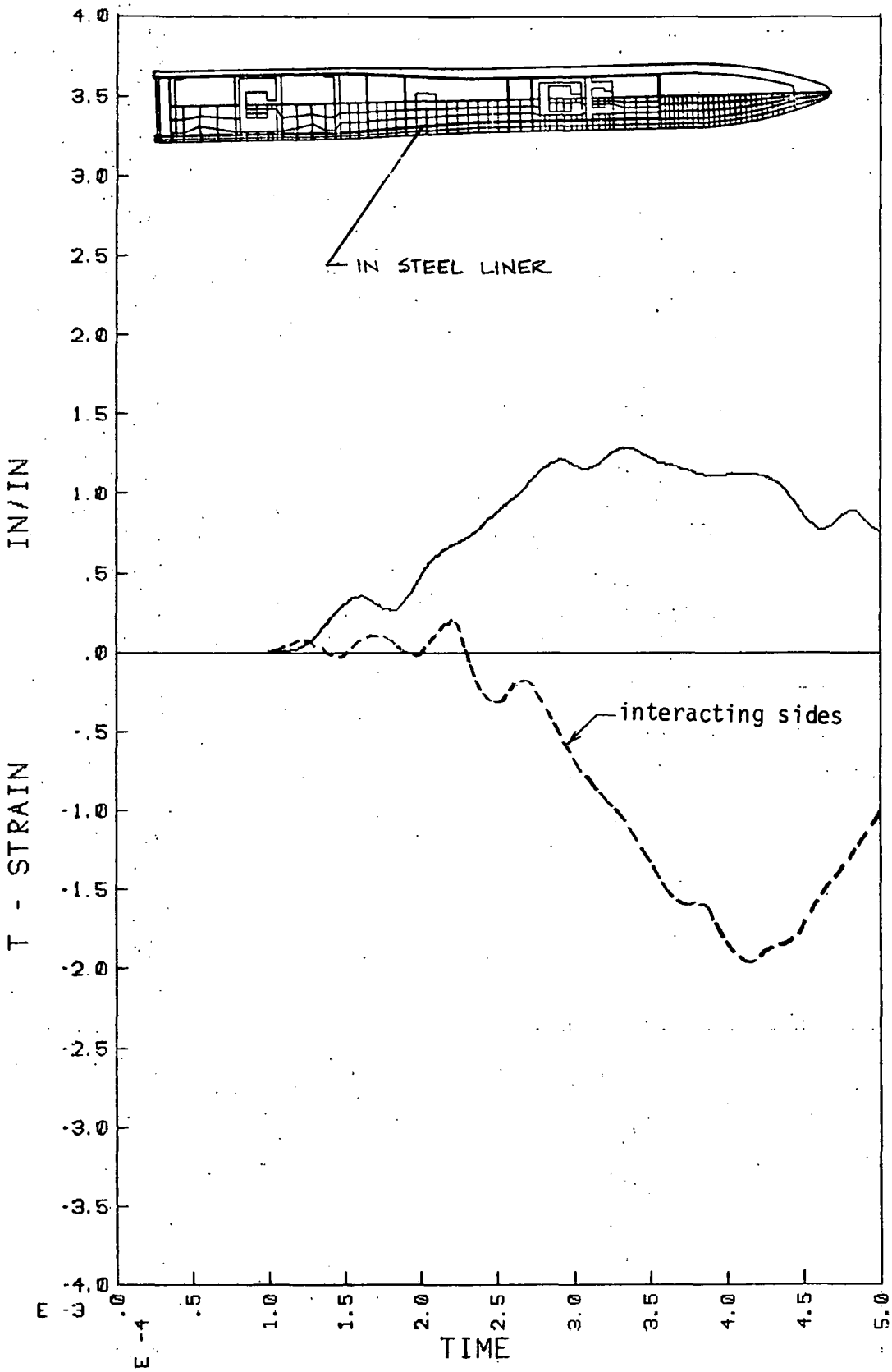

A7. Hoop strain in liner at taper.

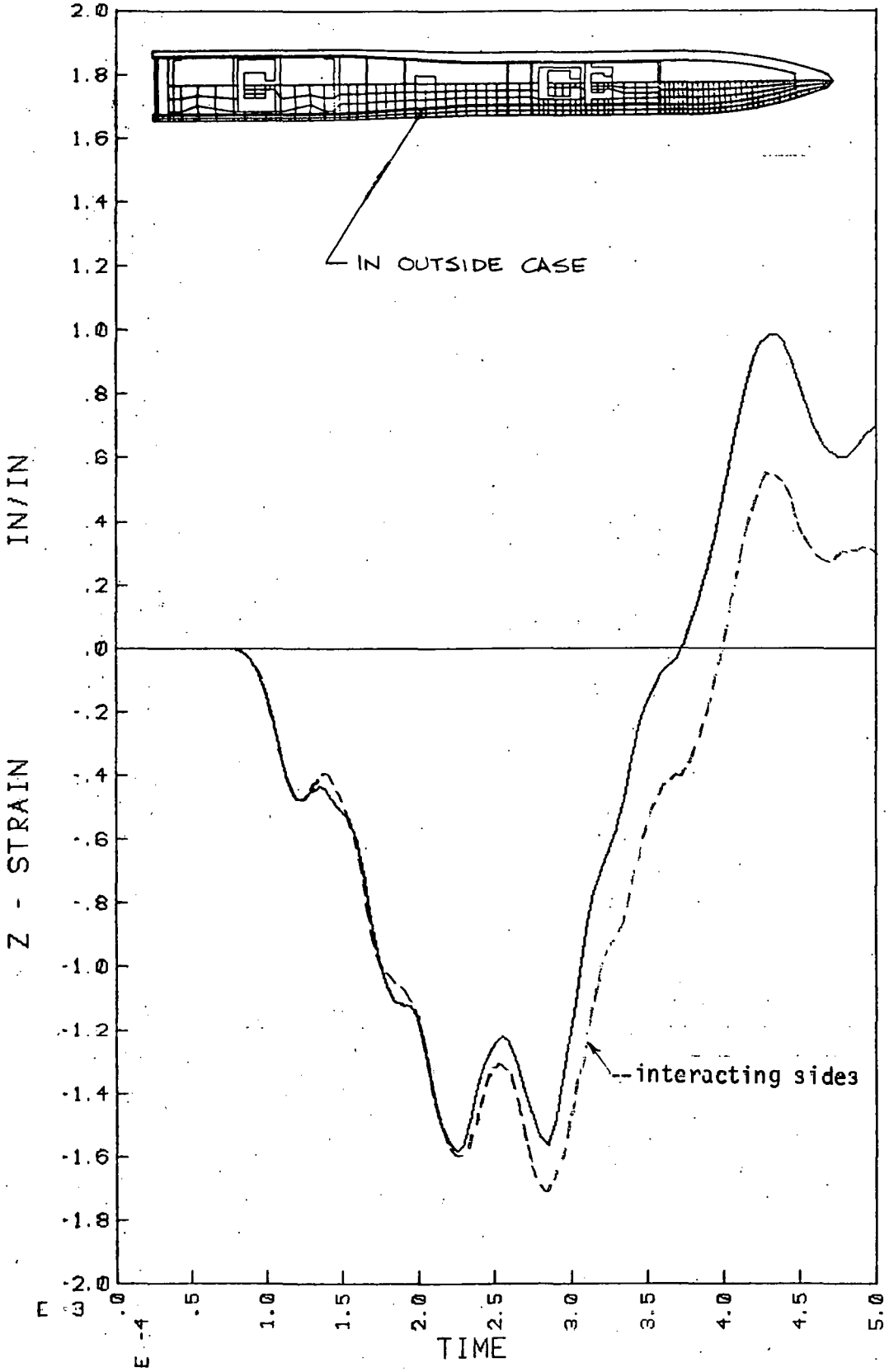

EP(DNA):514B (6/07/76) DYN (25MLOADSTPS)
ELEMENT 476

A8. Axial strain in outer case at taper.

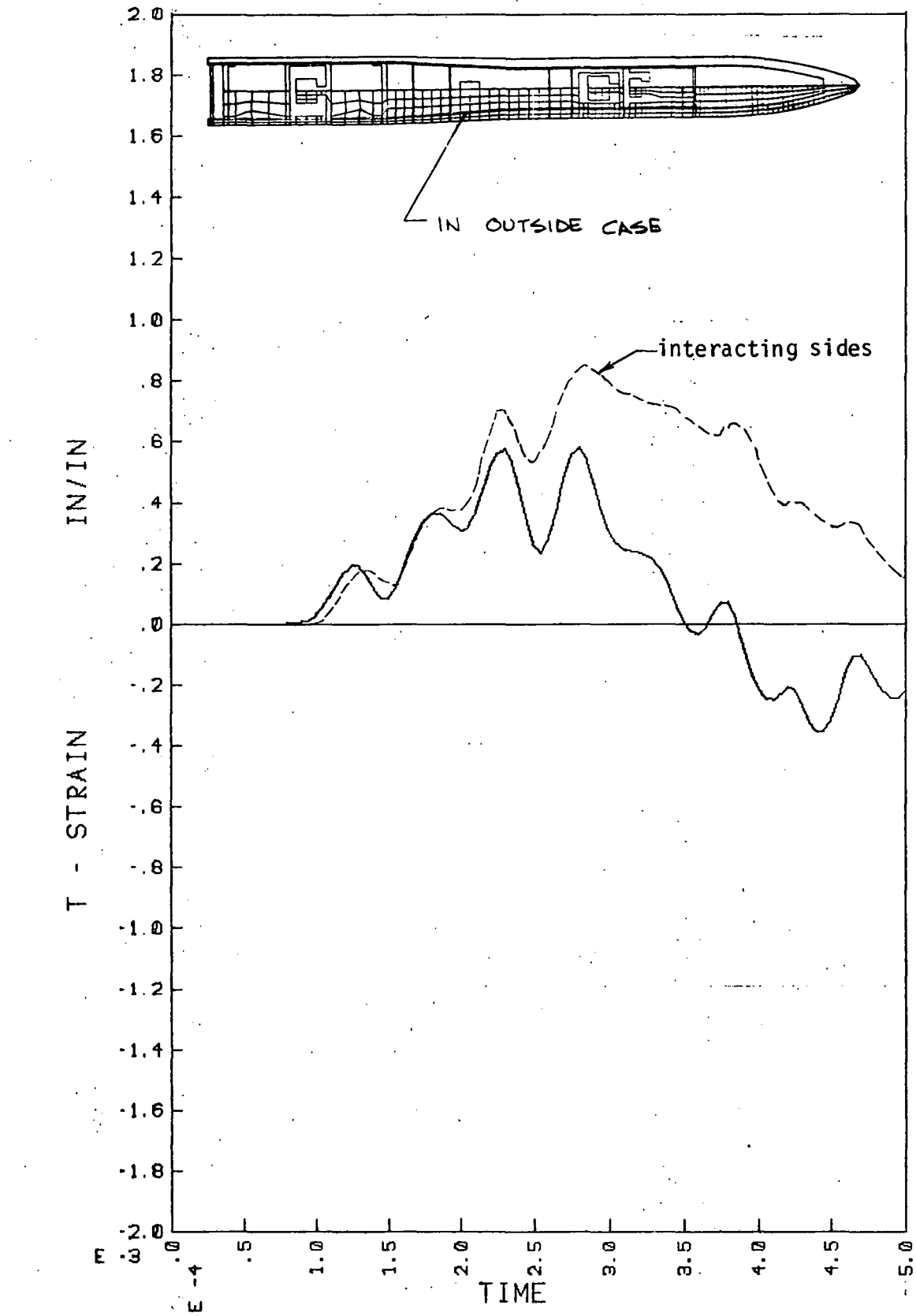

EP(DNA):514B (6/07/76) DYN (25MLOADSTPS)
ELEMENT 476

A9. Hoop strain in outer case of taper.

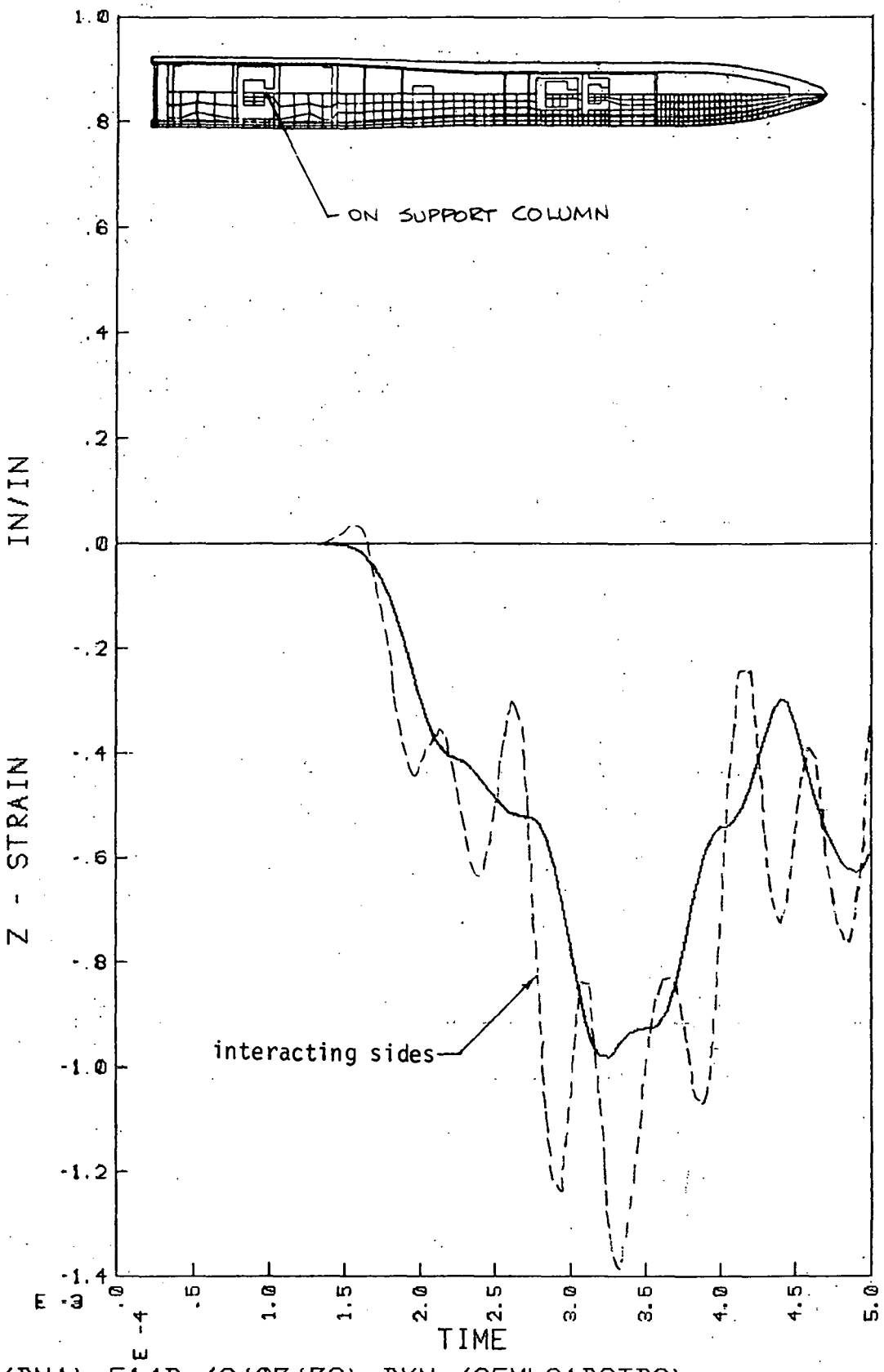

EP(DNA):514B (6/07/76) DYN (25MLOADSTPS)
ELEMENT 606

A10. Axial strain in support column of rear mass.

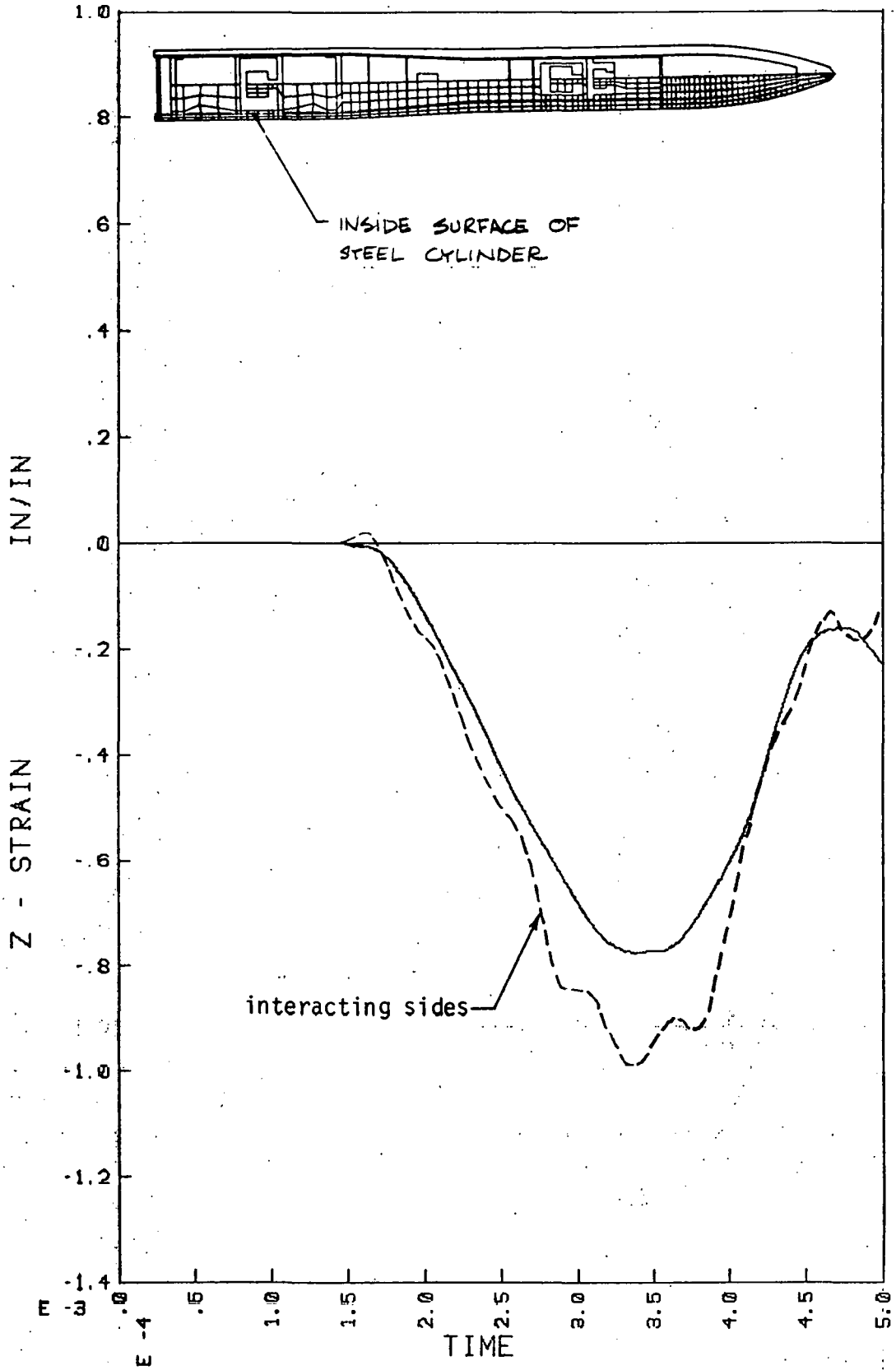

EP(DNA):514B (6/07/76) DYN (25MLOADSTPS)
ELEMENT 625

All. Axial strain in side wall of inner rear box.

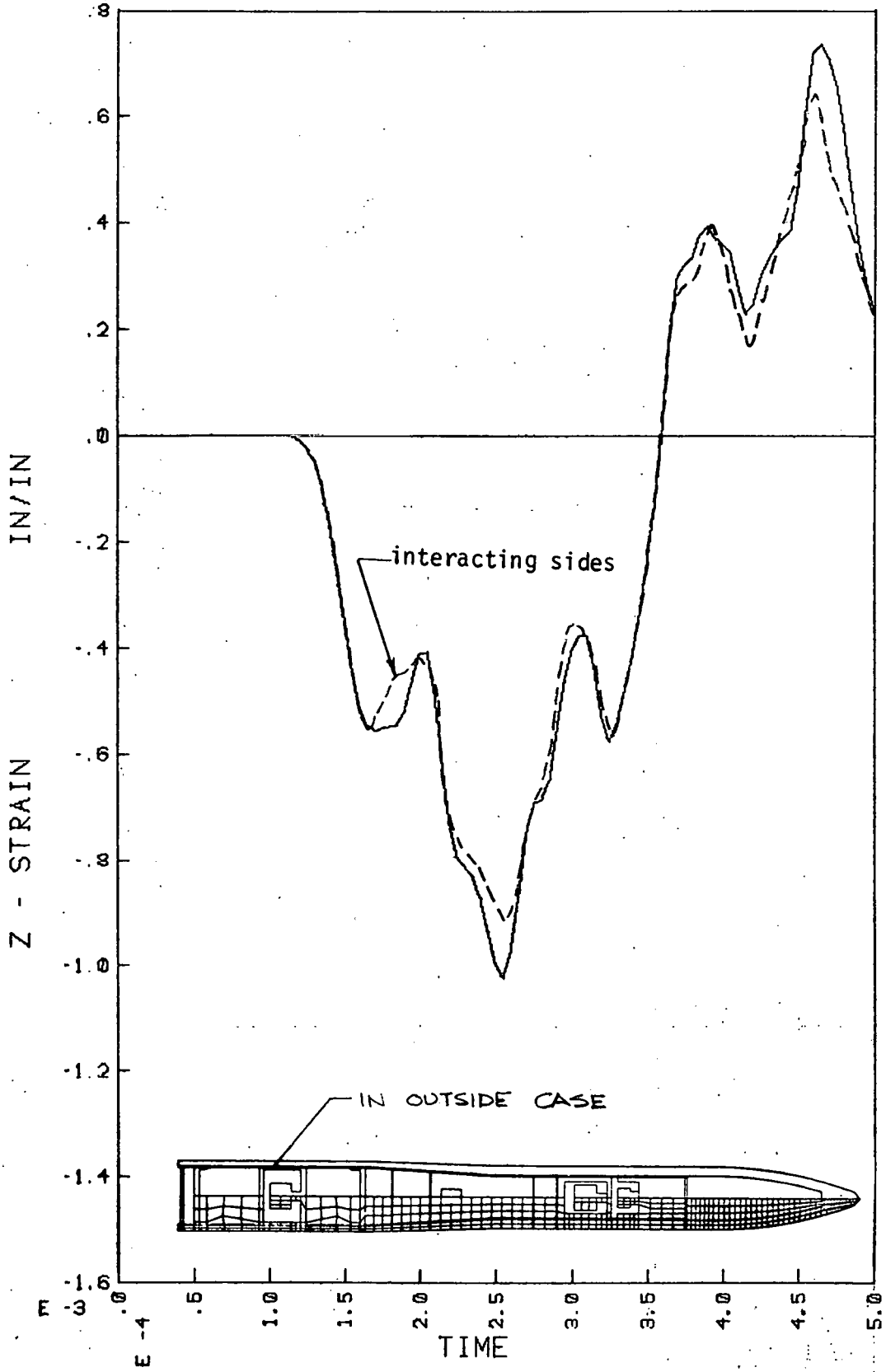

EP(DNA):514B (6/07/76) DYN (25MLOADSTPS)
ELEMENT 630

A12. Axial strain in outside case adjacent to rear box.

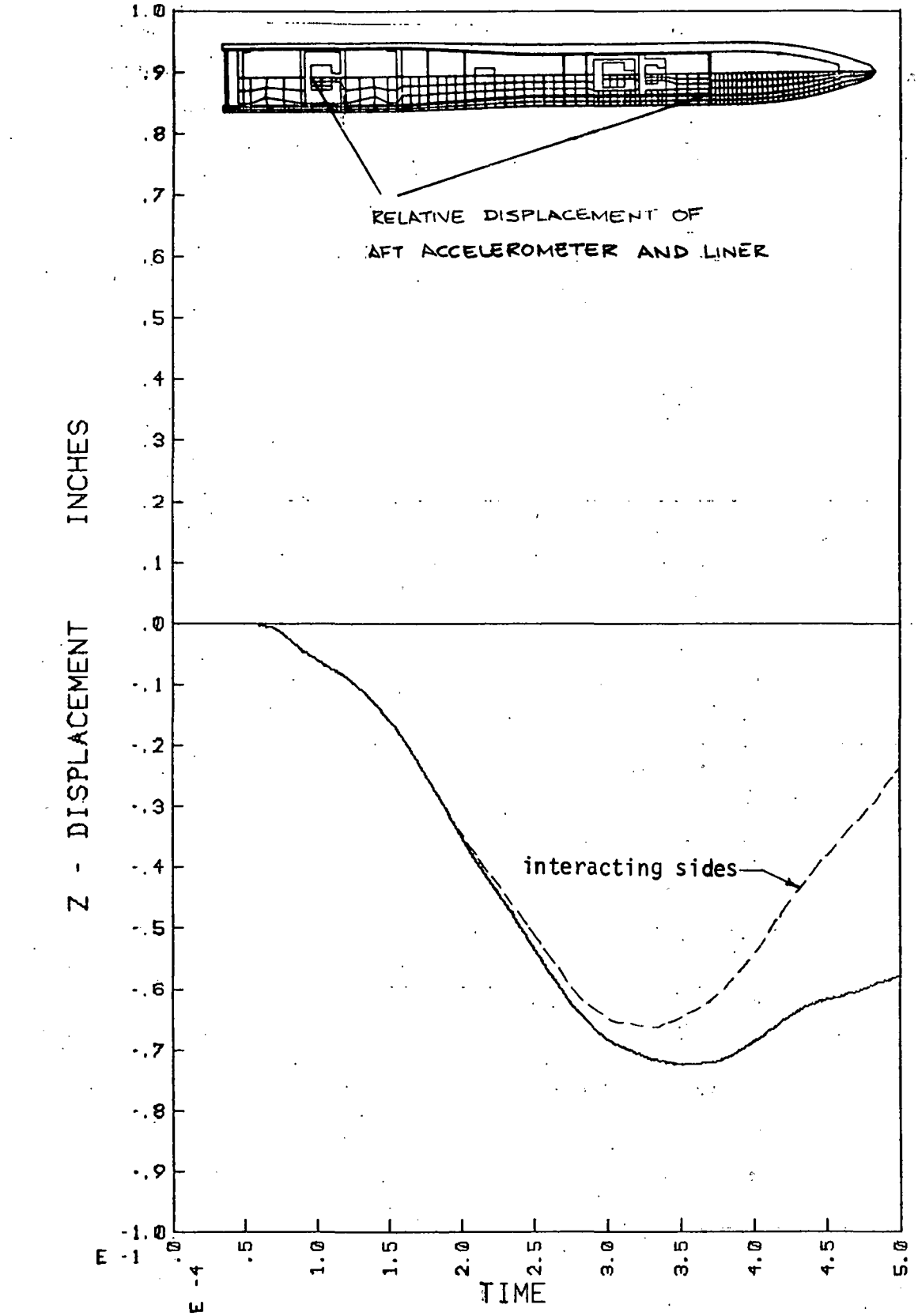

A13. Relative axial displacement of aft accelerometer and forward end of liner.

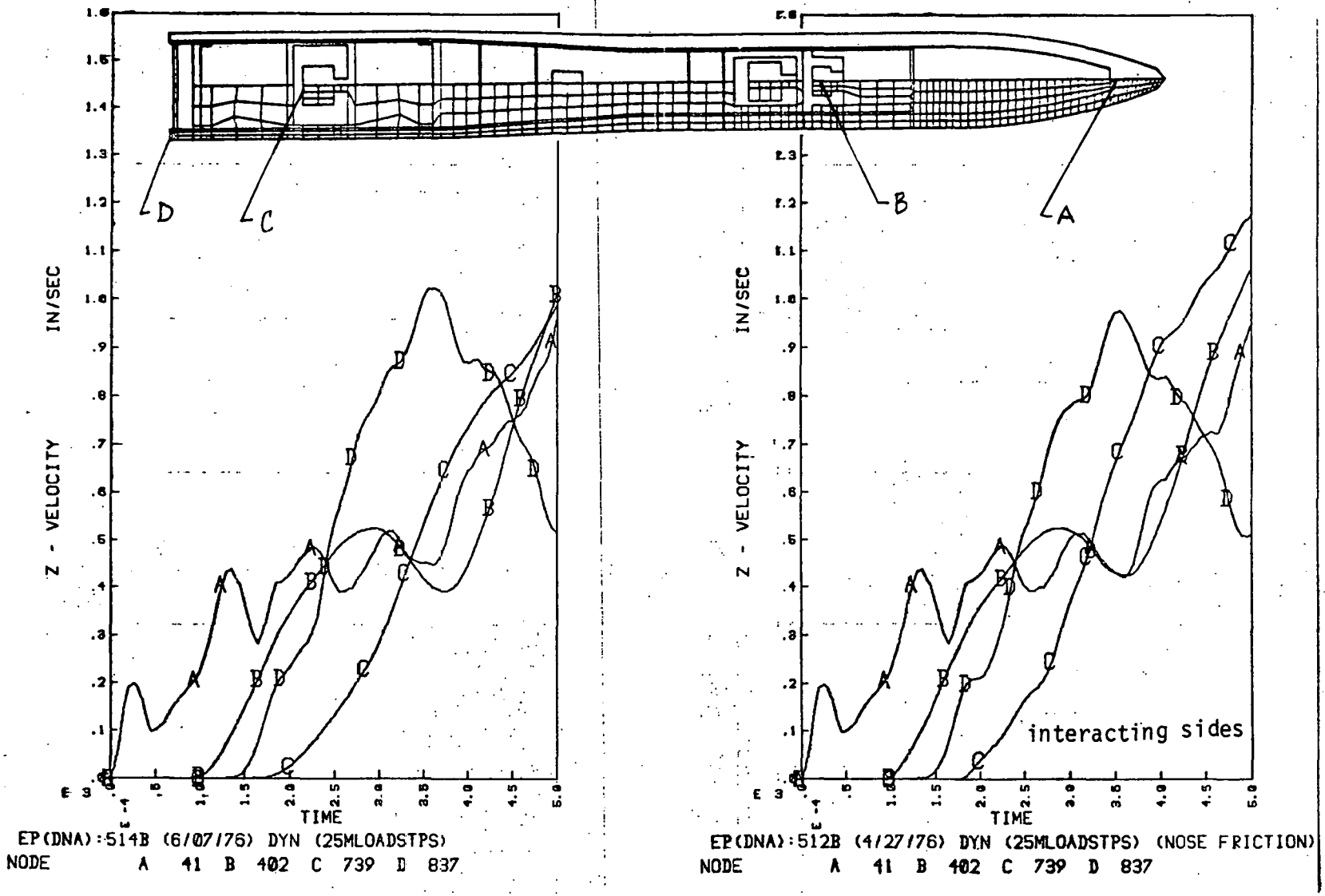

B1. Axial velocities of principal structure stations.

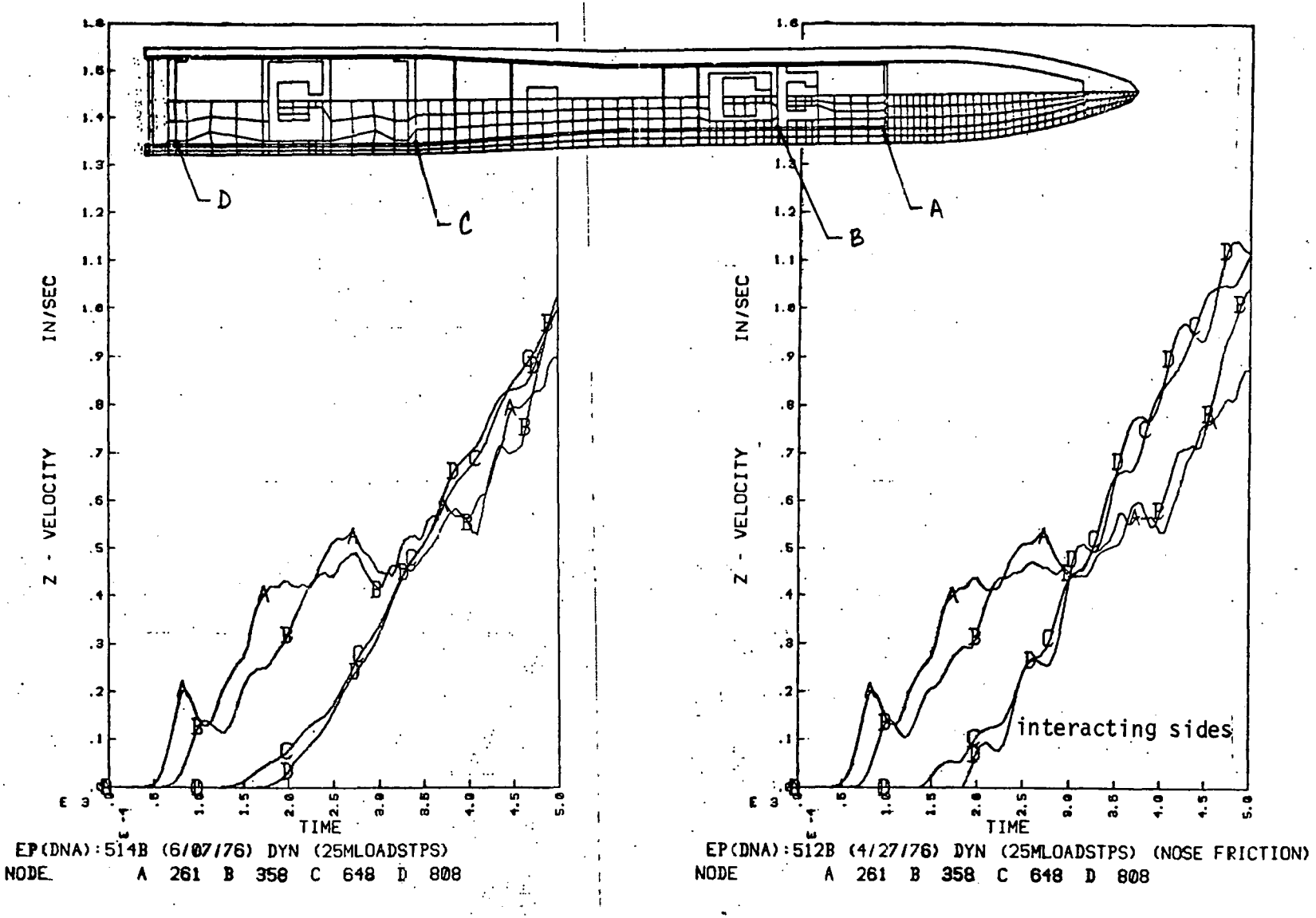

B2. Axial velocities of stations along liner.

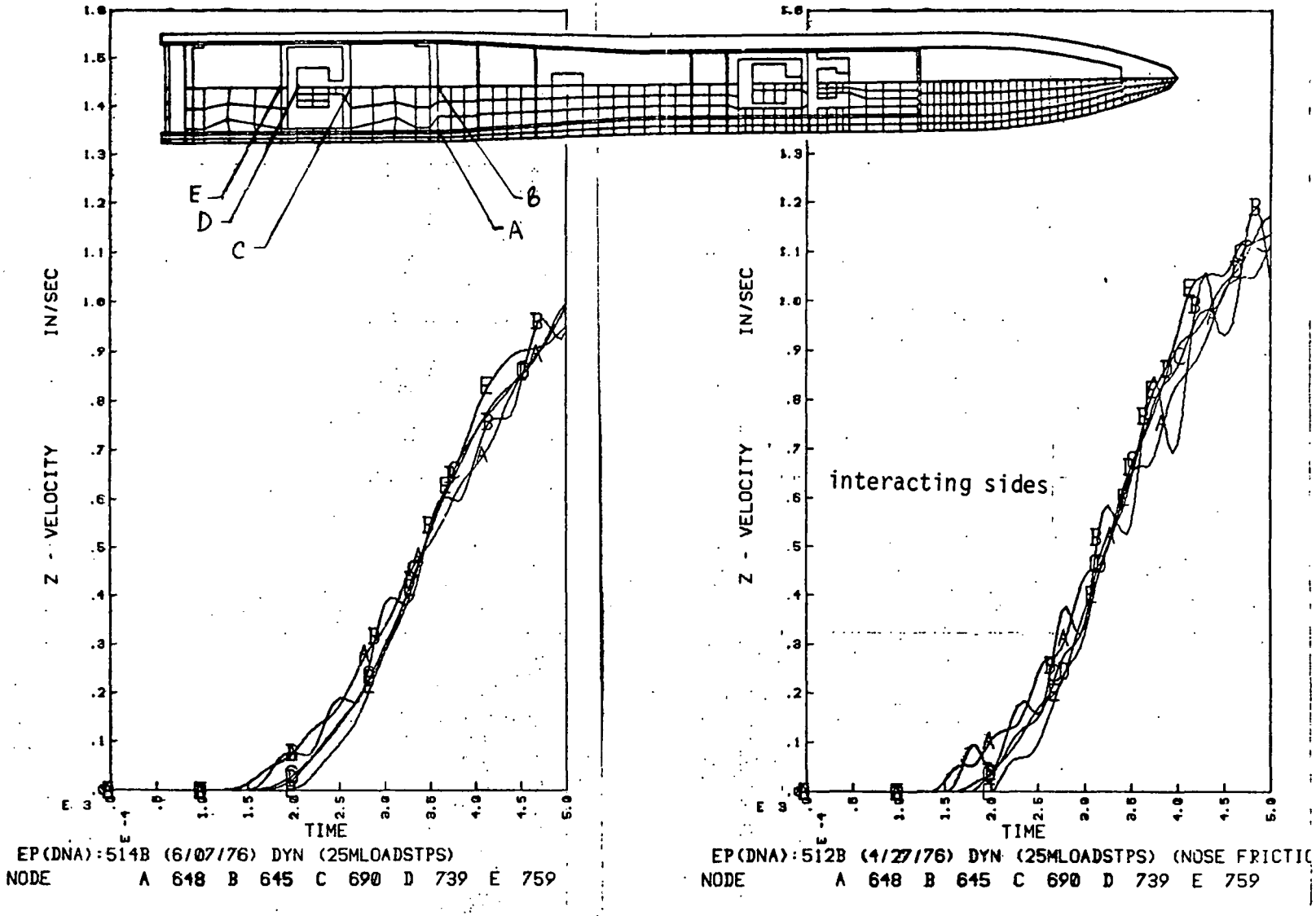

B3. Axial velocities of points in rear assembly.

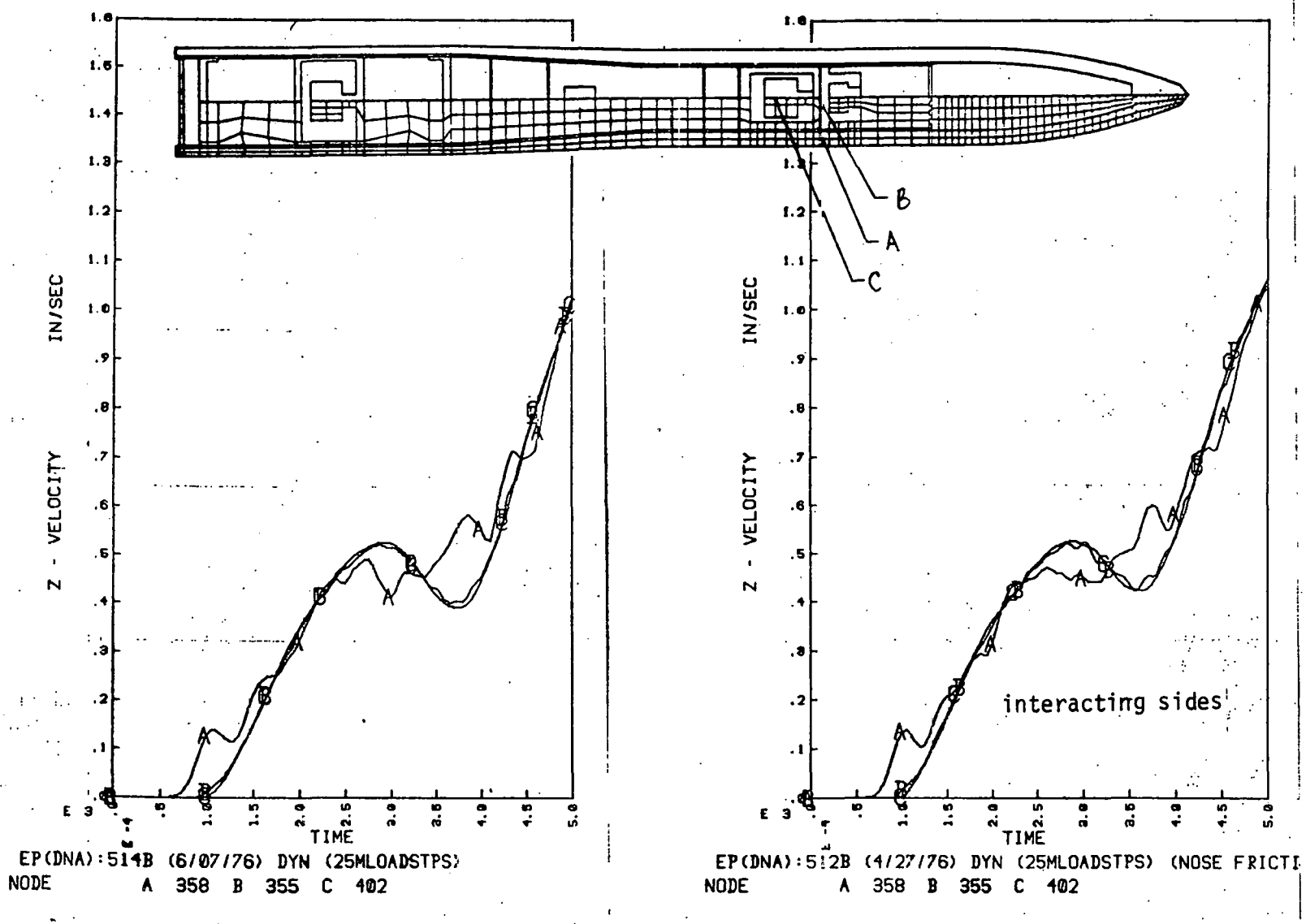

B4. Axial velocities of points in front assembly.

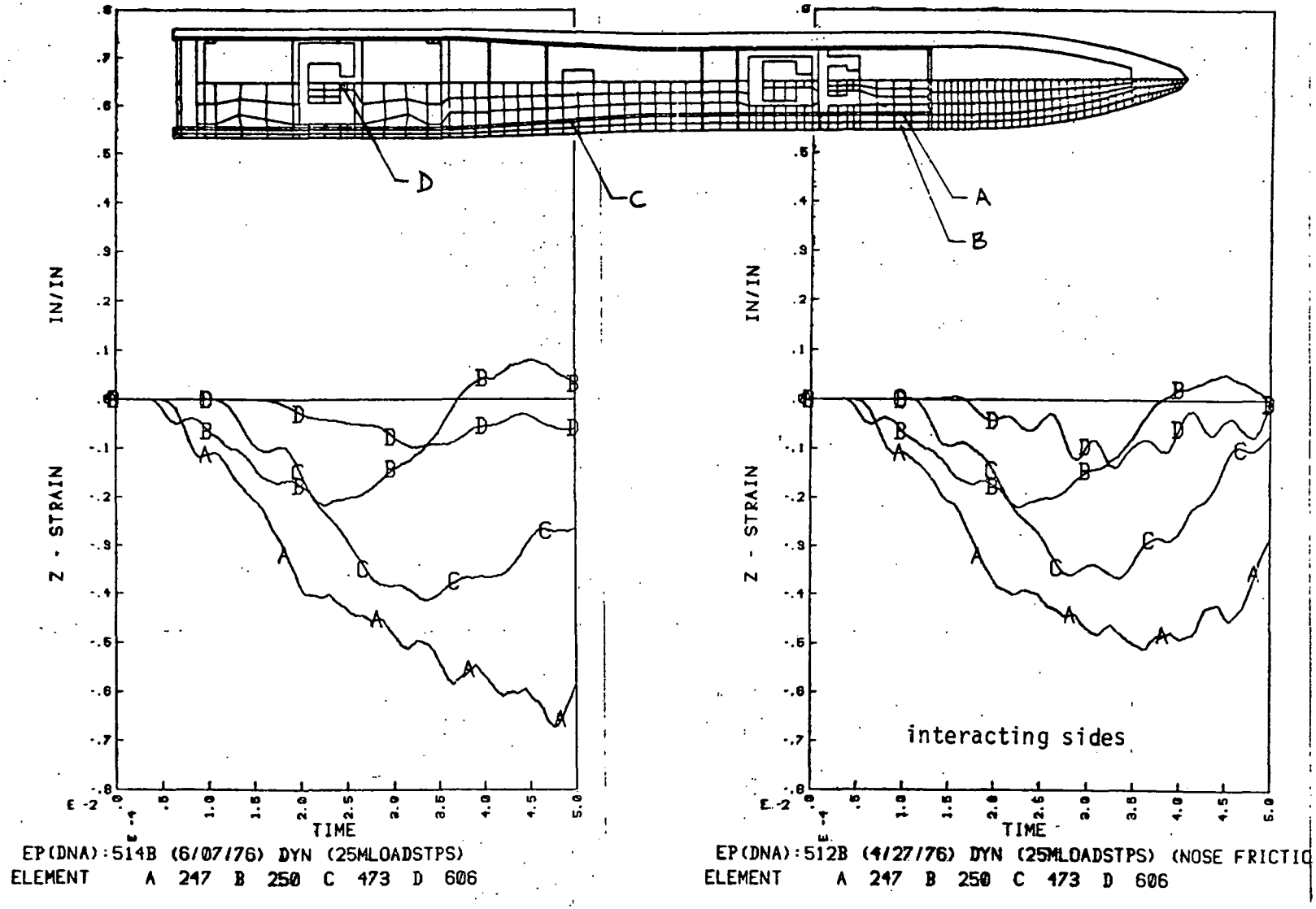

B5. Axial strains at key locations.

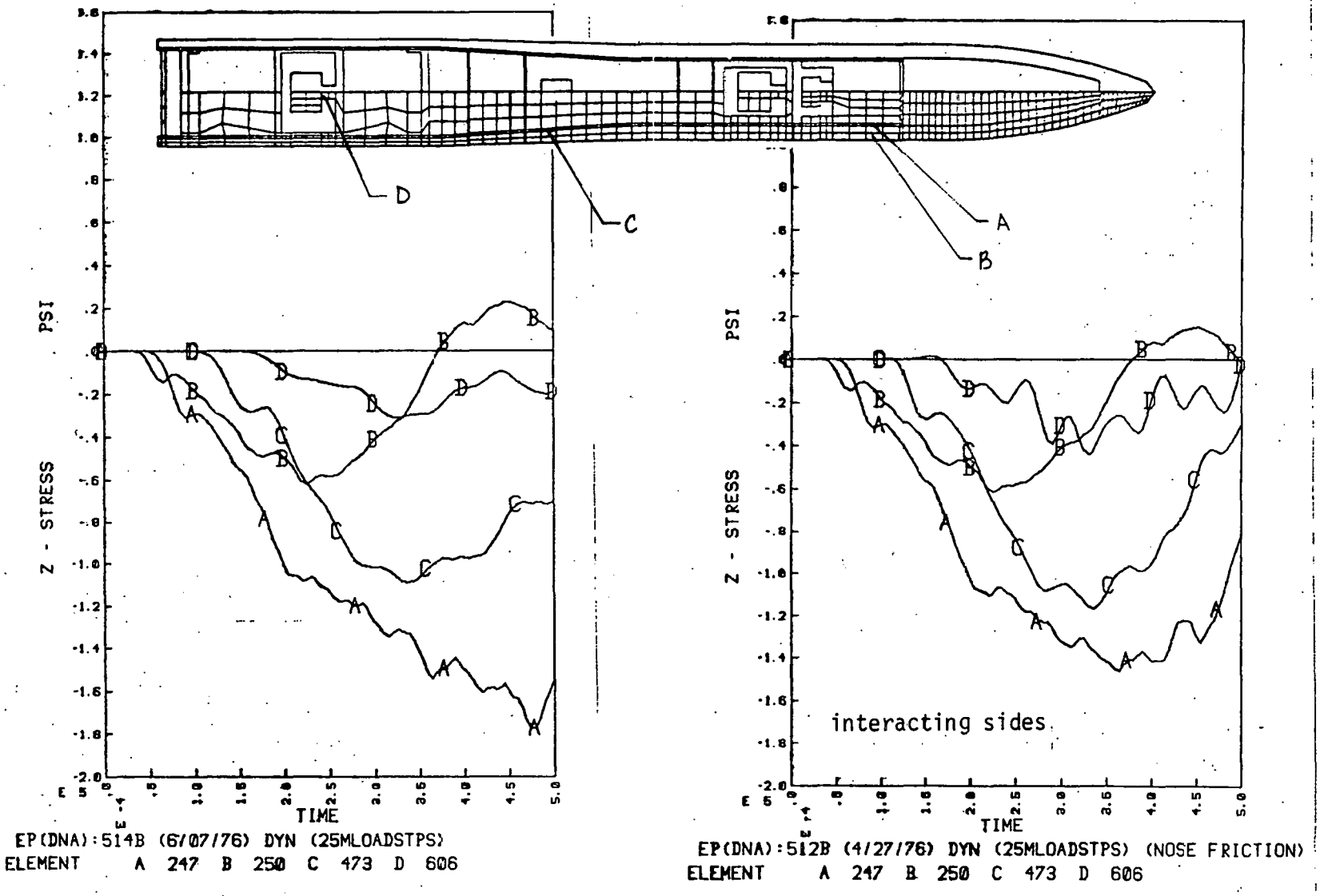

B6. Axial stresses at same locations.

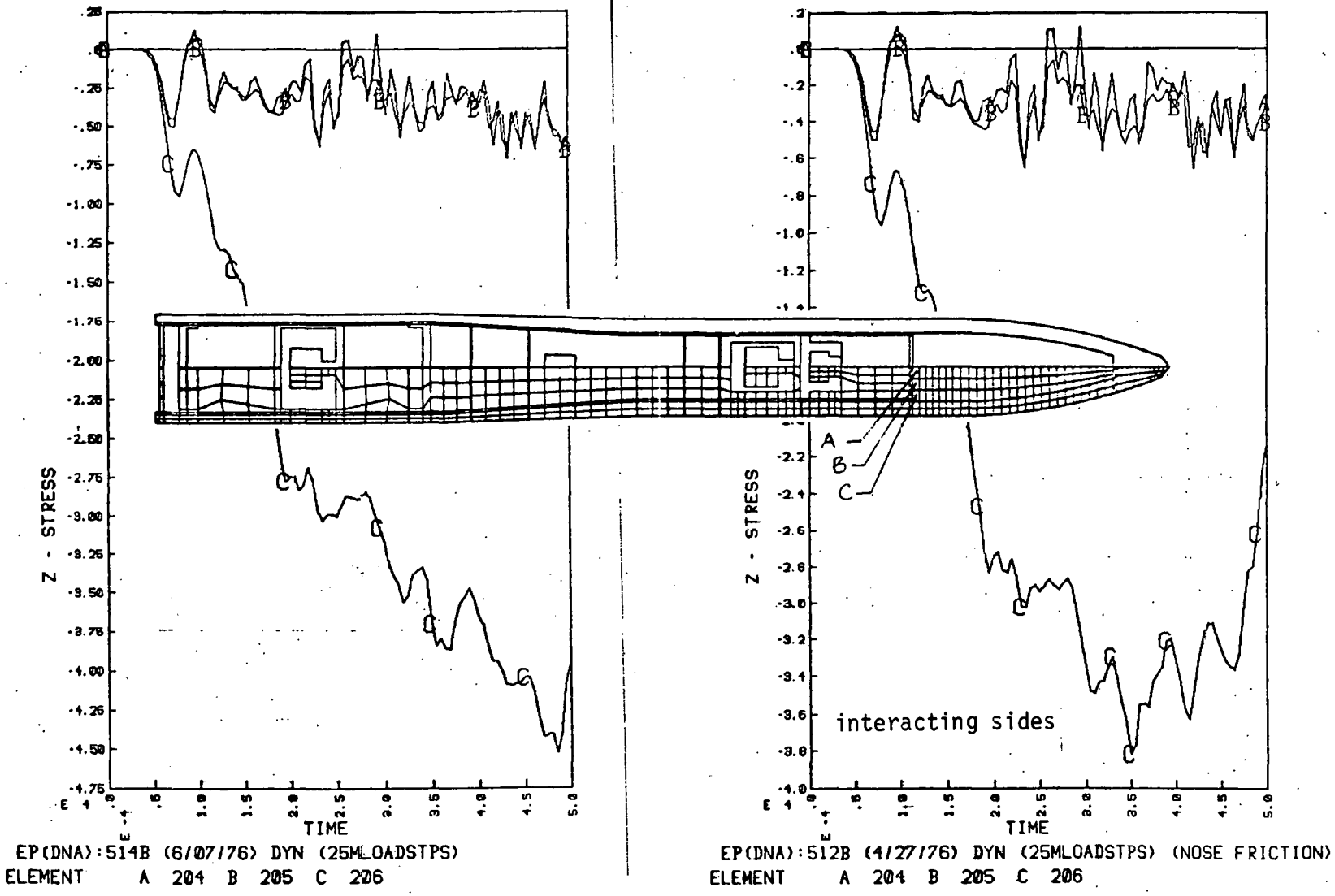

B7. Axial stress distribution at rear interface of ballast.

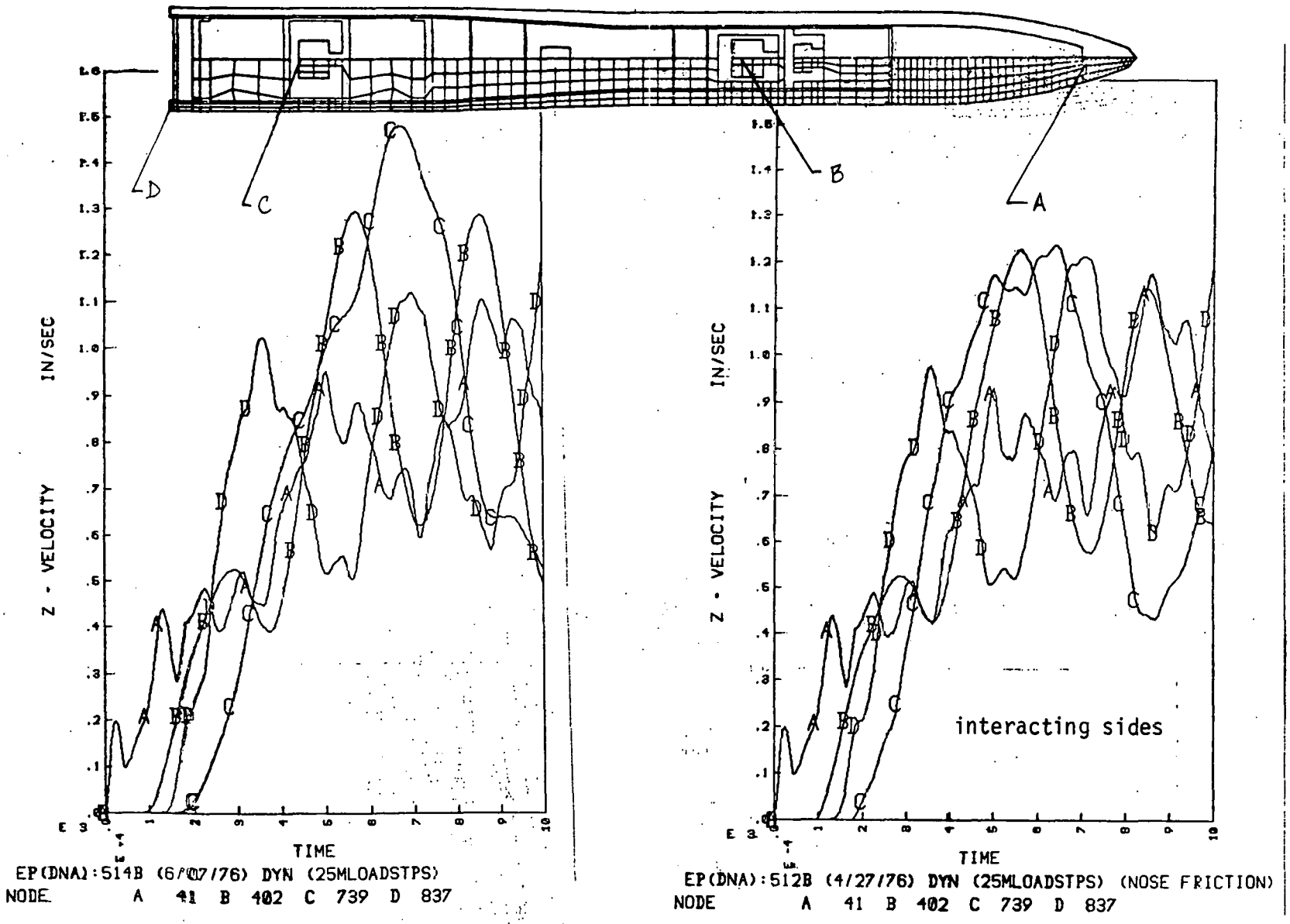

C1. Axial velocities of principal structure stations.

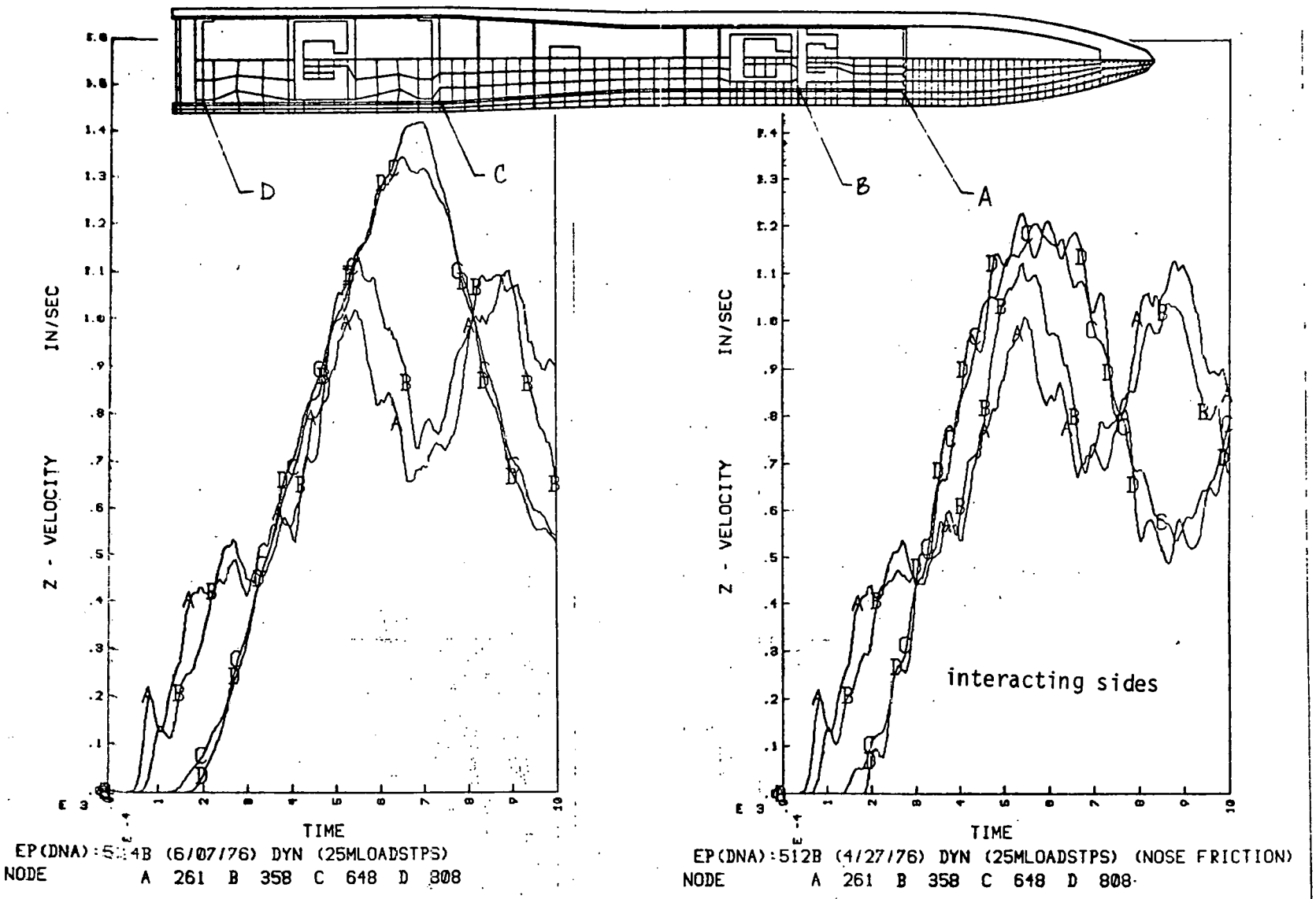

C2. Axial velocities of stations along liner.

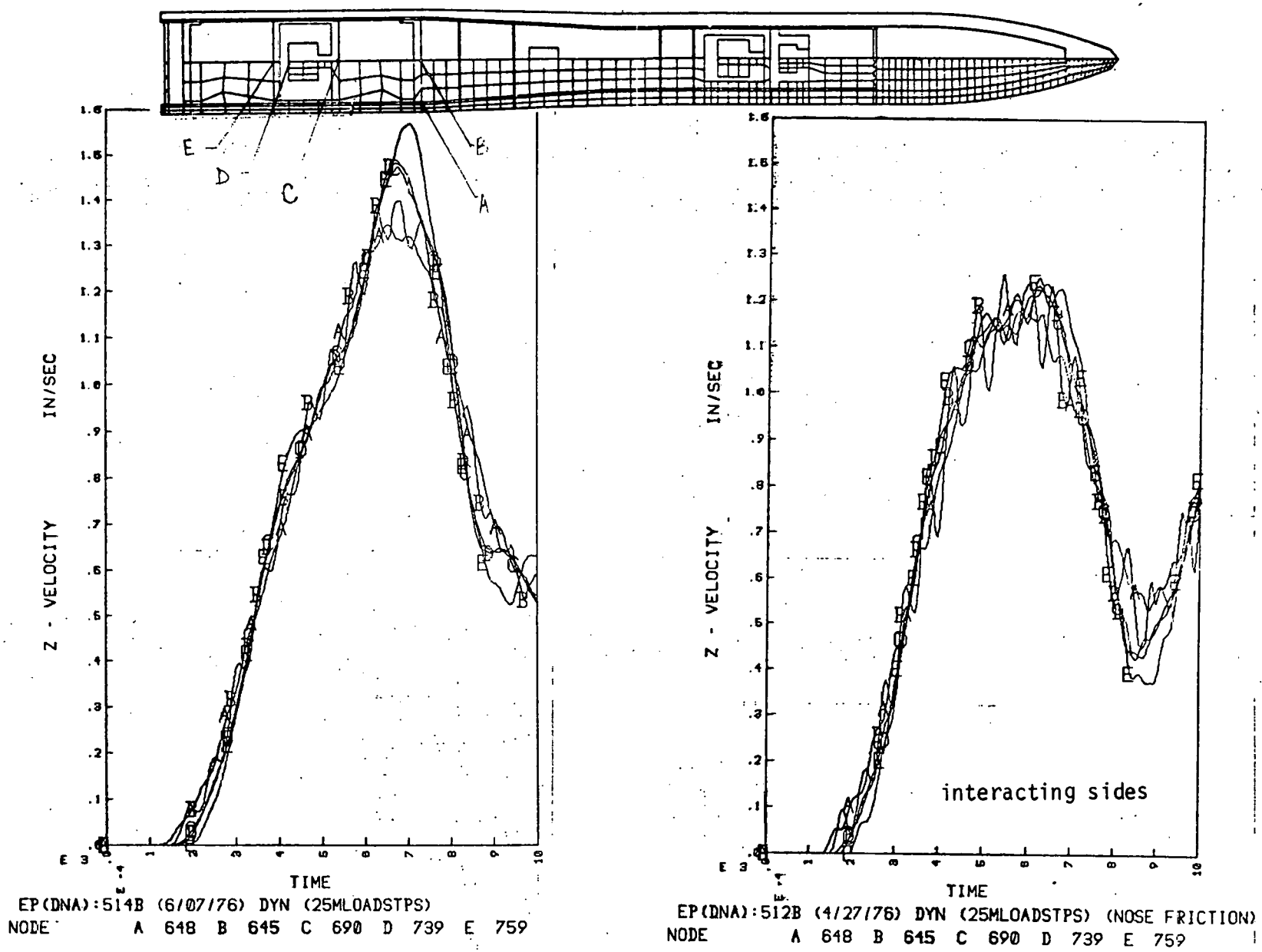

C3. Axial velocities of points in rear assembly

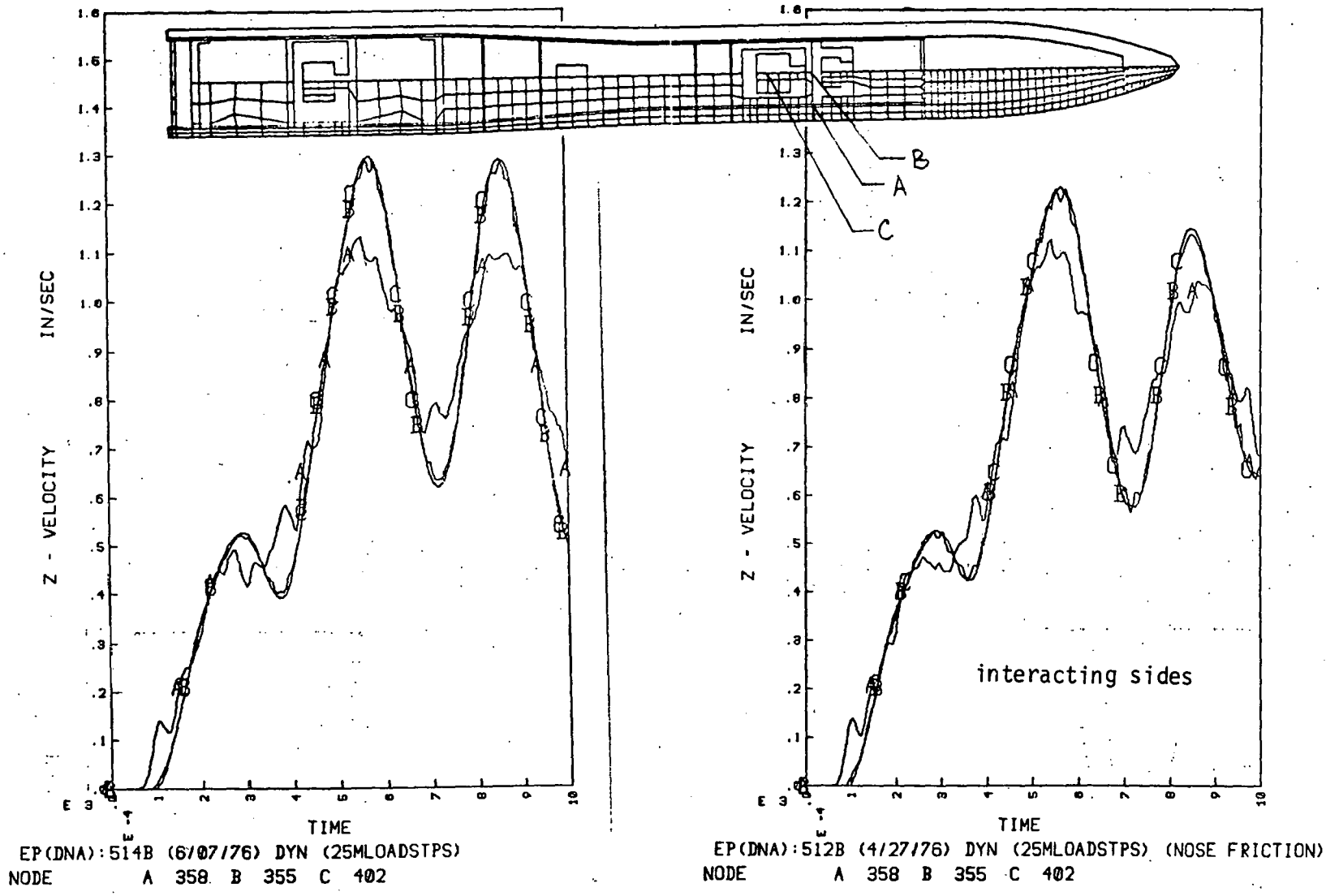

C4. Axial velocities of points in front assembly.

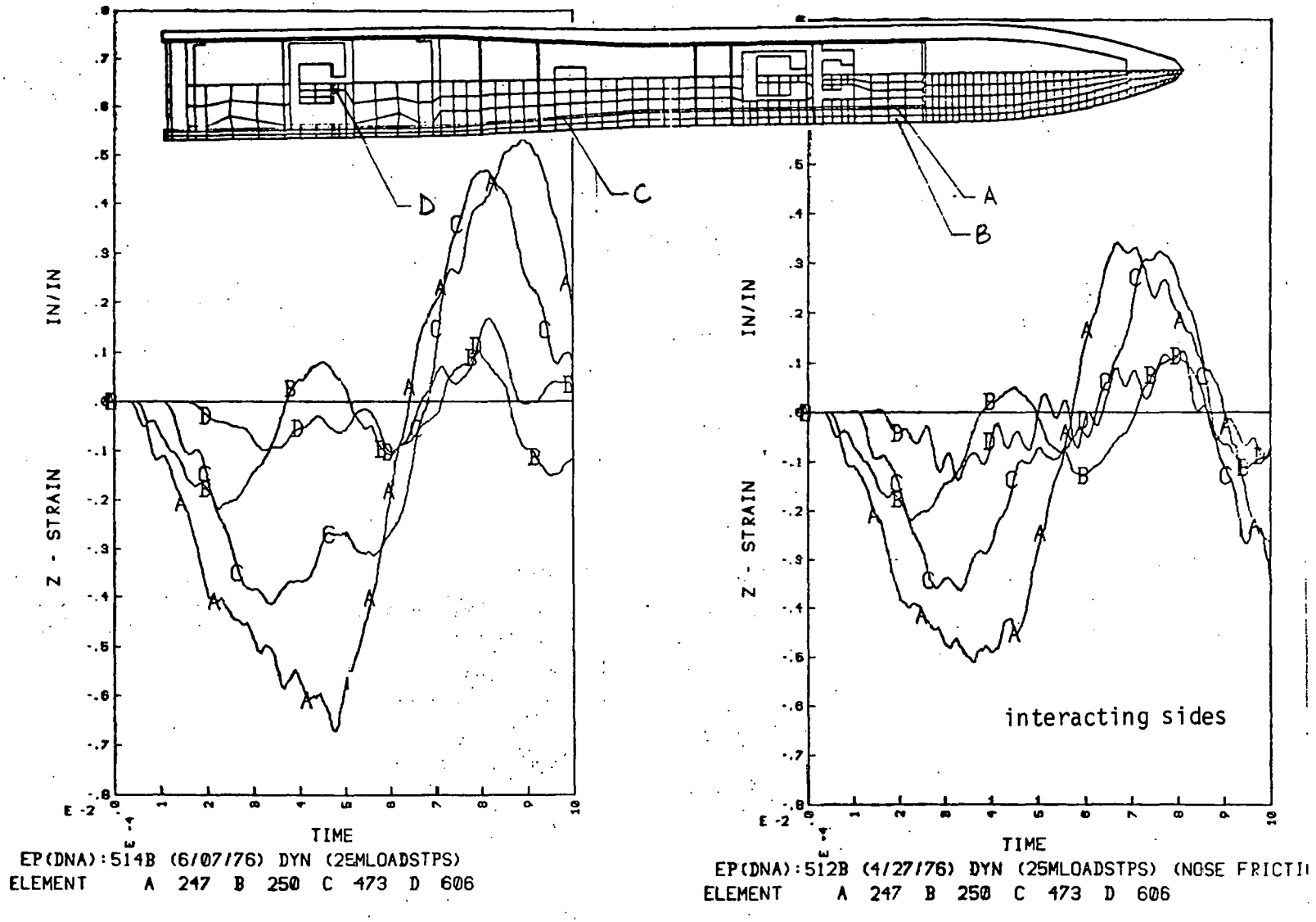

C5. Axial strains at key locations.

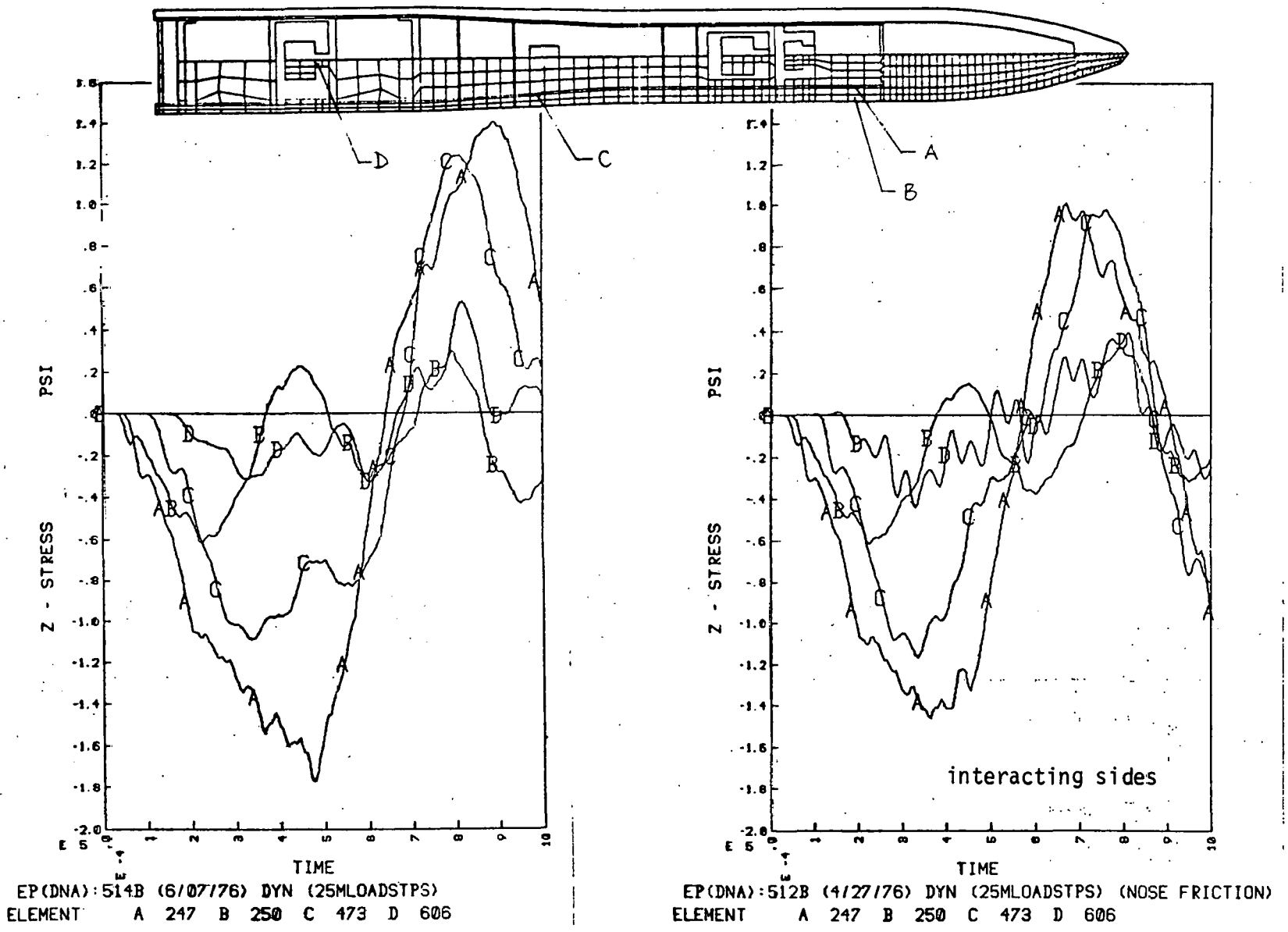

C6. Axial stresses at same locations.

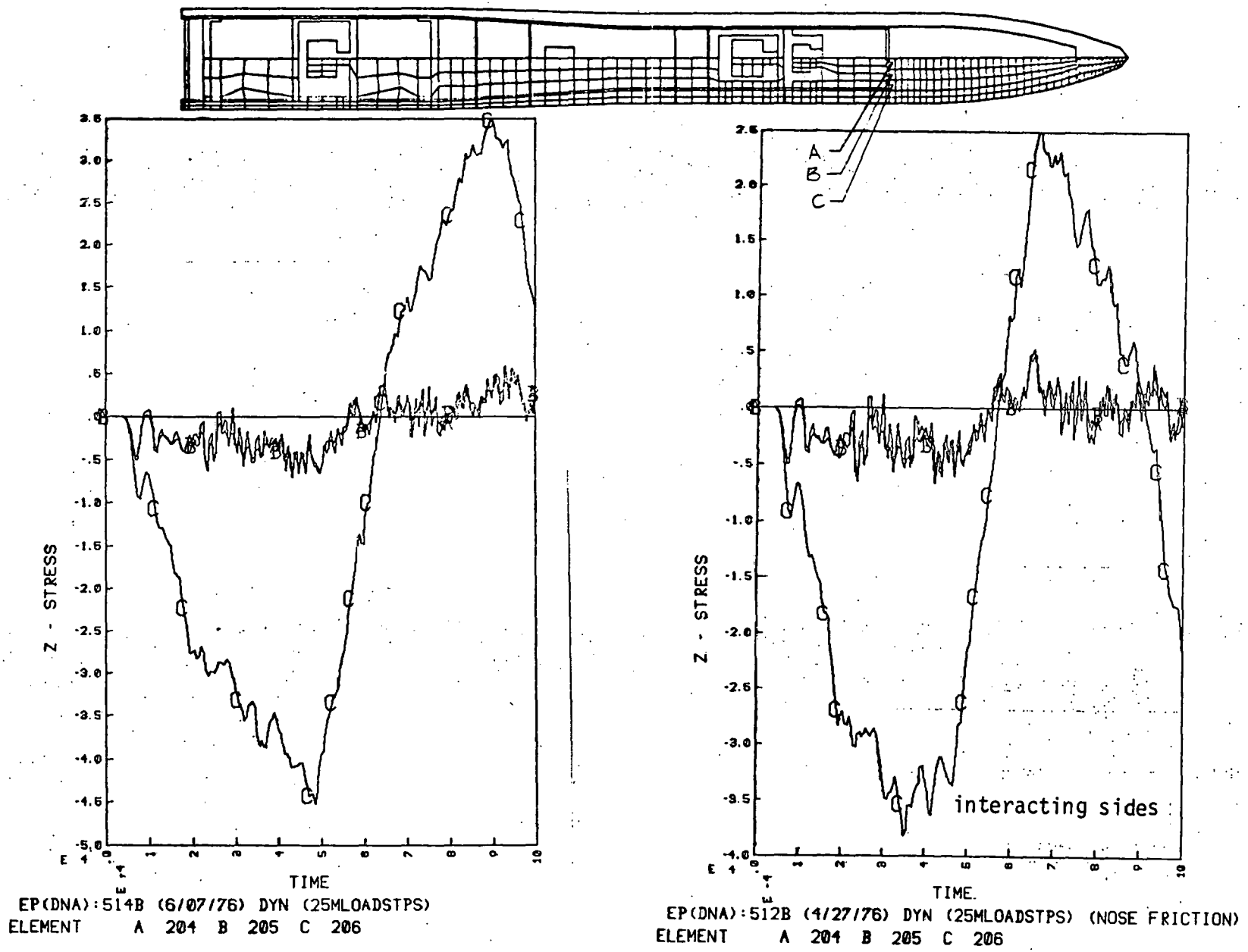

C7. Axial stress distribution at rear interface of ballast.

Printed in the United States of America
Available from
National Technical Information Service
U.S. Department of Commerce
5285 Port Royal Road
Springfield, VA 22161
Price: Printed Copy $; Microfiche $2.25

Page Range	Domestic Price	Page Range	Domestic Price
001–025	$ 3.50	326–350	10.00
026–050	4.00	351–375	10.50
051–075	4.50	376–400	10.75
076–100	5.00	401–425	11.00
101–125	5.25	426–450	11.75
126–150	5.50	451–475	12.00
151–175	6.00	476–500	12.50
176–200	7.50	501–525	12.75
201–225	7.75	526–550	13.00
226–250	8.00	551–575	13.50
251–275	9.00	576–600	13.75
276–300	9.25	601–up	*
301–325	9.75		

*Add $2.50 for each additional 100 page increment from 601 to 1,000 pages: add $4.50 for each additional 100 page increment over 1,000 pages.

Technical Information Department
LAWRENCE LIVERMORE LABORATORY
University of California | Livermore, California | 94550